EXPERIMENTAL AND MODELING STUDIES OF DENDRITE INITIATION DURING LITHIUM ELECTRODEPOSITION

by

ADAM M. MARASCHKY

Submitted in partial fulfillment of the requirements

for the degree of Doctor of Philosophy

Thesis Advisor: Professor Rohan Akolkar

Department of Chemical & Biomolecular Engineering

CASE WESTERN RESERVE UNIVERSITY

August, 2020

CASE WESTERN RESERVE UNIVERSITY

SCHOOL OF GRADUATE STUDIES

We hereby approve the dissertation of

Adam Maraschky

candidate for the degree of Doctor of Philosophy*.

Committee Chair

Prof. Rohan Akolkar

Committee Member

Prof. Uziel Landau

Committee Member

Prof. Donald Feke

Committee Member

Prof. Alp Sehirlioglu

Date of Defense

May 7, 2020

*We also certify that written approval has been obtained

for any proprietary material contained therein.

DEDICATION

For those who gave everything to fight the outbreak of COVID-19.

May their sacrifices never be forgotten.

TABLE OF CONTENTS

LIST OF TABLES

LIST OF FIGURES

ACKNOWLEDGEMENTS

I give my sincere thanks to my research advisor, Professor Rohan Akolkar, for his mentorship over the last four years. While I greatly appreciate the opportunity to work on such an important and interesting topic, I also appreciate his attention to my personal and professional development. I cannot imagine my graduate education without his encouragement along the way. For all the times I felt lost or unsure, he was there to nudge me back on the right path. I will always value the discipline he imparted on me: thinking critically about what is known vs. unknown, prioritizing what is most important, and simplifying ideas so that others can easily understand them.

I also need to thank my committee members, Professors Uziel Landau, Donald Feke, and Alp Sehirlioglu. Their thoughtful questions and probing insights motivated me to be clear about my assumptions, dig deeper into my topic, and focus the scope of my research to realistic goals.

This work would not have been possible without financial support from the Ohio Federal Research Network (OFRN) through the Center for Excellence on 'Partnership for Research in Energy Storage and Integration for Defense and Space Exploration (PRESIDES)'. Partial financial support was also given by the Great Lakes Energy Institute (GLEI) ThinkEnergy Fellowship.

There are a number of others at CWRU whom I would also like to thank: Mark Haberbusch and the rest of the GLEI staff, the ThinkEnergy Fellows, the staff at Sears

ThinkBox, Evan Guarr and the rest of the staff and faculty of the Chemical & Biomolecular Engineering Department, as well as the many students I had the pleasure of getting to know. I am grateful for the contributions my peers made beyond the curriculum, both socially and professionally, through the Chemical Engineering Graduate Student Organization (ChEGSO) and the Electrochemical Society (ECS) Student Chapter.

I have appreciated working amongst talented research group members: Lu Y., Jacob B., Sherry L., Kailash V., Dai S., Ryan G., Darshika J., Katie S., Jack G., Nora S., Bethany K., Peilun Z., and Mahesh I. We share a special comradery through fundamental discussions during group meetings. We aim for high standards of safety and cleanliness in the lab. We ask tough questions. The group culture we share has been an integral part of my graduate experience. May these practices continue for many years!

I thank my parents for their deep love and support throughout my life. I also thank them for their sacrifices for my education and growth. I appreciate their patience and understanding always, even when I insisted that I do things my way.

I treasure the companionship and care of my wife, Emily, who has been by my side since the beginning of this journey. Her steadfast love provides me strength and her work ethic is a constant source of inspiration.

Lastly, I give thanks and praise to the Lord God Almighty. Soli Deo gloria.

LIST OF SYMBOLS

C	Concentration, mol cm^{-3}
$\mathcal{D}$	Diffusion coefficient cm^2 s^{-1}
F	Faraday constant, 96485 C mol^{-1}
i	Current density, mA cm^{-2}
L	SEI thickness, nm
$\dot{L}$	SEI growth rate, nm s^{-1}
n	Number of electrons transferred, $n = 1$ for Li
Q	Charge density, C cm^{-2}
Q_{s}	Constant phase element
R	Resistance, Ω cm^{-2}
T	Temperature, ℃
t	Time variable, s
t_+	Transference number of the positive species
V	Applied voltage, V

Greek

α	constant in film growth law
α_{c}	Cathodic charge transfer coefficient
δ	Liquid phase boundary layer thickness, cm
ε	Plating efficiency
η	Overpotential, V
κ	Ionic conductivity, S cm^{-1}
σ	Duty cycle
τ	Time constant, s

Subscripts and Superscripts

0	Initial or bulk value
$*$	Normalized to the initial value
$+$	Positive ion species
b	Bulk, outside boundary layer
c	Cathode
diff	Diffusion process
e	Electrode surface (C_e); electrolyte (R_e)
flat	At the 'flat' portion electrode surface
L	Limiting, in the liquid phase
liq	Refers to the liquid phase
off	Open circuit conditions, while current is 0
on	During plating, while current is on
onset	Onset of dendrite growth
plate	Plating, when cathodic current is passing
s	Working electrode surface
SEI	Refers to the solid electrolyte interphase
soak	Electrode contacts electrolyte at open circuit
tip	At the tip of a dendrite precursor

Experimental and Modeling Studies of Dendrite Initiation during Lithium Electrodeposition

Abstract

by

ADAM M. MARASCHKY

High-energy density batteries are essential for powering future electric vehicles (EVs) and electric aircraft. These technologies are limited by the capacity of their batteries. Enabling high-specific energy batteries could make longer-range electric vehicles and electric aircraft a reality. The Li-metal anode offers the highest theoretical specific energy among practically available anode materials. However, secondary Li-metal anodes experience capacity loss and safety hazards caused by the growth of dendrites on the anode surface during charging. After four decades of research on Li-metal batteries, rechargeable Li-metal anodes that do not evolve dendrites are still not commercially available. Understanding the physical causes and mechanisms of dendritic Li electrodeposition, in order to develop commercial Li-metal batteries, motivates the present work.

It is shown herein that solid-state transport limitations within a dynamic solid electrolyte interphase (SEI) are dominant in controlling the time when Li dendrites first form. Chronopotentiometry and optical imaging provide experimental observations for when dendrites first appear on a Li electrode. Dendrite onset time is shown to increase with increasing temperature and decrease with increasing current density and initial SEI thickness. These phenomena are shown to be due to the onset of diffusion limitations brought on by a thickening SEI. Electrochemical impedance spectroscopy (EIS) provides

evidence for SEI growth and enables estimation of the SEI growth rates during Li electrodeposition. These experiments guide the development of an analytical model that explains mechanistically how transport limitations within the SEI control the onset time of dendrite growth during Li electrodeposition. The model also provides predictions of Li dendrite onset times. These predictions agree qualitatively with the observed effects of current density, initial SEI thickness, temperature, and pulsing. Finally, it is shown through numerical modeling that pulsed current (p.c.) plating is not able to mitigate the concentration depletion experienced at the Li electrode in a way that would prevent dendrites during the charging of Li-metal batteries. At an equivalent-plating rate, the increased SEI growth rate and decreased plating efficiency negate the benefits of concentration profile relaxation provided by p.c. plating.

CHAPTER 1. Introduction

1.1 Motivation: To Enable High-Energy Density Li-Metal Batteries

High-energy density batteries are essential for powering future electric vehicles (EVs) and electric aircraft.[1] These technologies, as well as many other mobile electronics, are limited by the energy capacity of their power sources. Engineers face a tradeoff between weight and capacity when selecting a battery: greater capacity requires a heavier and bulkier battery. One of the longest-range electric vehicles to date, the Tesla Model S 100D, offers 390 miles per charge. This range is made possible by a 100 kWh Li-ion battery pack that is ~1300 lb (roughly 1/3 of the total vehicle weight).[2,3] One approach to overcome the capacity-weight tradeoff is to develop energy storage technologies which hold more energy per mass. These high-specific energy, rechargeable batteries could make longer-range electric vehicles and electric aircraft a reality.

Li-ion batteries (LIBs) are used in the vast majority of today's EVs. They consist of a layered graphite intercalation anode and a layered Li_xMO_2 cathode (where M is Co, Fe, Ni, Mn or their combinations) sandwiching a porous separator soaked in nonaqueous electrolyte (Fig. 1.1).[4] When a LIB is charged and discharged, Li^+ cycles back and forth between the anode and the cathode, de-inserting itself from one and intercalating into the other.[5] State-of-the-art LIBs offer an energy density of ~200 Wh/kg.[6] This technology has become ubiquitious for its relatively high-specific energy density (compared to ~40 Wh/kg for Pb-acid) and its rechargeability (long cycling life).

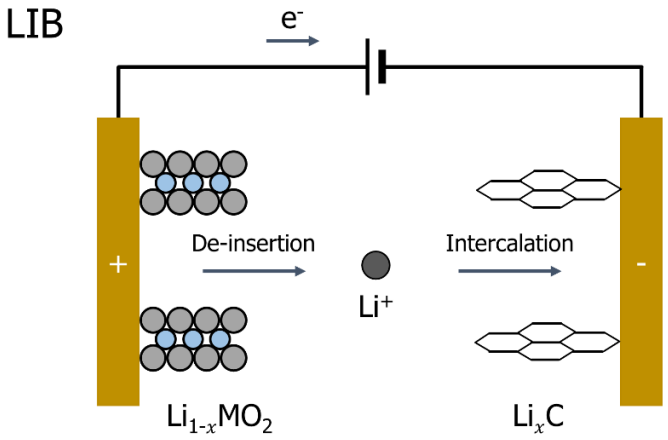

Anode	$C + x\ Li^+ + x\ e^- \longrightarrow Li_xC$
Cathode	$LiMO_2 \longrightarrow Li_{1-x}MO_2 + x\ Li^+ + x\ e^-$
Overall	$LiMO_2 + C \longrightarrow Li_xC + Li_{1-x}MO_2$

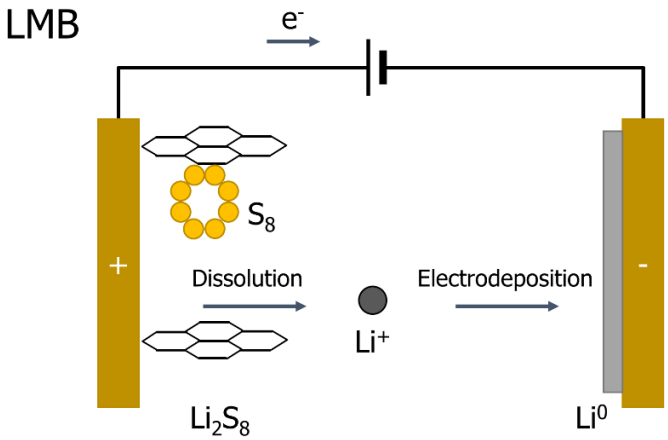

Anode	$Li^+ + e^- \longrightarrow Li^0$
Cathode	$Li_2S_8 \longrightarrow S_8 + 2\ Li^+ + 2\ e^-$
Overall	$Li_2S_8 + \longrightarrow 2Li^0 + S_8$

Figure 1.1 - Schematics of Li-ion (LIB) and Li-metal batteries (LMB) during charging with their respective reactions shown below. Li-S (*bottom*) is an example of LMB.

Li-metal batteries (LMBs), such as Li-S and Li-O_2, have a thin metallic Li anode instead of the intercalation anode (Fig 1.1). The Li-metal anode offers significantly higher theoretical specific energy than both Li-ion and Zn-metal (Fig. 1.2).[7] This is due to the the low mass density of Li-metal (0.53 g cm^{-3}) and the high cell voltages enabled by the Li reduction potential (−3.0 V vs. SHE). While primary (non-rechargeable) Li-metal batteries have been available for years, the commercial development of secondary Li-metal anodes has been hindered by capacity loss and safety hazards caused by the growth of dendrites on the anode surface during charging (Fig. 1.3).[8-14]

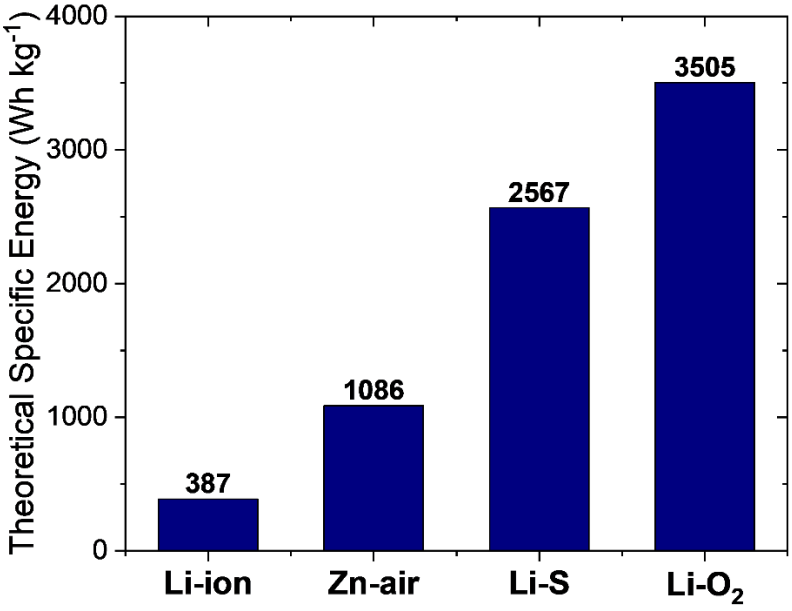

Figure 1.2 - Theoretical specific energy of several secondary battery chemistries.[7] The intercalation graphite anode of Li-ion batteries sacrifices specific energy for greater dimensional stability. Li-S and Li-O_2 are examples of Li-metal battery chemistries. Zn-air batteries feature a metal Zn anode in aqueous electrolyte.

Figure 1.3 - A lithium foil electrode covered with dendrites after Li electrodeposition.

The development of the LIB was originally motivated by the demand to make Li batteries safely rechargeable by eliminating dendrites.[15] However, the graphite intercalation anode used in the Li-ion battery design sacrifices specific energy in order to gain safety and reliability.[4,7] Understanding the physical causes and mechanisms of dendritic Li electrodeposition, in order to develop commercial LMBs, motivates the present work.

1.2 Prior Lithium Dendrite Models and Suppression Strategies

Classical models for dendrite growth during electrodeposition of metals provide a foundation for understanding Li dendrites. In 1961, Barton and Bockris developed the first theoretical model for dendrite growth rates.[16] Their work on Ag electrodeposition established equations for the velocity of dendrite tip growth under mass transport and surface energy control. This model explains the mechanism underlying dendrite growth

during electrodeposition in aqueous electrolytes. As shown in Fig. 1.4, when the cathodic reaction depletes the concentration of cations at the electrode surface, dendrites grow due to spherical diffusion at the tip of pre-existing nodules or bumps (Fig. 1.4). The increased diffusion to the tip releases it from concentration overpotential, locally enhancing the current density (reaction rate), and thereby promoting dendrite growth.[17] This model was later refined by Diggle *et al.* based on Zn electrodeposition experiments. They provided details about dendrite initiation as a transition from pyramidal growth under linear-diffusion control to a spherically-shaped tip under activation control.

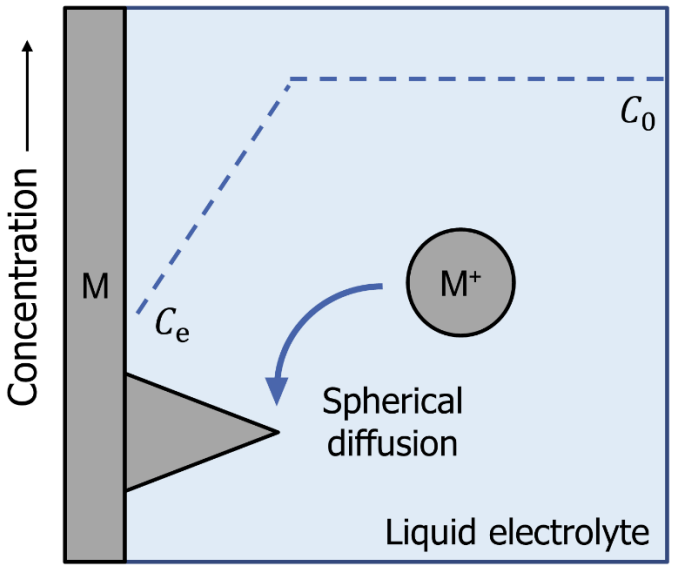

Figure 1.4 - Classical mechanism for dendrite growth in liquid electrolytes. As metal ions (M^+) are consumed at the metal surface (M), the near-surface concentration (C_e) decreases relative to the bulk concentration (C_0). The reaction at the flat surface of M experiences diffusion limitations, whereas the tip of a dendrite experiences spherical diffusion, which releases it from transport limitations. Thus, the reaction rate at the dendrite tip is limited only by activation and surface energy. The disparity in the local current densities (reaction rates) promotes dendritic growth.

Monroe and Newman modified the Barton and Bockris model to describe Li dendrite propagation in polymer electrolytes.[18] Akolkar adapted the mathematical model of Monroe and Newman to liquid electrolytes and incorporated concentration dependence of the Li^+ diffusion coefficient.[19] The above models share the same core principle: dendrite growth during electrodeposition is promoted by a release from concentration overpotential. However, previous dendrite models do not explain some of the peculiarities of lithium dendrites. The application of the Bockris models to Li electrodeposition is problematic because Li dendrites grow well below the limiting current (*e.g.*, ~1% of the limiting current density i_{L}),

$$i_{\mathrm{L}} = \frac{nF\mathcal{D}_{\mathrm{liq}}C_{\mathrm{b}}}{\delta(1-t_+)} \qquad [1.1]$$

Here, n is the number of electrons transferred, F is the Faraday constant 96485 C mol^{-1}, $\mathcal{D}_{\mathrm{liq}}$ is the diffusion coefficient in the liquid electrolyte (~10^{-5} cm^2 s^{-1}), C_{b} is the bulk concentration of the reacting species, t_+ is the transference number of the Li^+ species, and δ is the boundary layer thickness. Typical values of i_{L} are ~100 mA cm^{-2}, yet Li dendrites grow below 0.5 mA cm^{-2} (see §2.2). According to the classical models, dendrite growth rates are expected to be very low when the current density is far below the limiting current. This enigma needs to be resolved, and greater clarity is needed about the role surface films play in the initiation of Li dendrites.

Dendrite formation when electrodepositing Li metal is strongly influenced by the presence of surface films, which spontaneously form on alkali metals.[9,20-22] Jorné and Tobias first demonstrated the feasibility of alkali metal electrodeposition in nonaqueous

electrolytes.[23] Scarr[24] and Dey[25] were among the first to investigate directly the surface films present on Li metal. In the late 1970s, Peled introduced the solid electrolyte interphase (SEI) model for alkali metal surface films and their growth.[26] By highlighting the importance of Li^+ transport through the surface layer, this model laid the foundation for understanding the unique electrochemical behavior of Li metal. Over the years, many investigators have characterized the composition, structure, growth, and transport properties associated with the SEI in a variety of electrolytes.[27-34] Direct evidence that the SEI influences the Li electrodeposit morphology was provided by Cohen and Aurbach, who performed *in-situ* AFM studies linking non-uniformities in the SEI to non-uniform Li deposition-dissolution.[35-37] Steiger *et al.* showed that SEI grows during electrodeposition, and cannot be removed during dissolution.[38] The influence of non-uniformities in the SEI thickness on Li dendrite propagation was modeled via continuum simulations by Liu and Lu.[39] In recent years, the mechanical action of a solid electrolyte in contact with the Li electrode and its efficacy in retarding dendrite propagation has been the subject of considerable study.[40-45]

Aside from the models and surface characterization mentioned above, significant work has been done to understand the initiation of Li dendrites by attempting to answer the following questions: when do Li dendrites initiate and what controls the dendrite onset time?[46-50] For example, Bai *et al.* noted that dendrites form when Li electrodeposition transitions from a reaction-limited to a diffusion-limited condition.[48] They found that the dendrite onset time scaled with the Sand time,[51]

$$\tau_s = \pi \mathcal{D}_{\text{liq}} \left[\frac{nF C_b}{2i(1 - t_+)} \right]^2 \qquad [1.2]$$

where i is the applied current density. Eq. 1.2 predicts the time for the concentration of the positively charged species (*e.g.*, Li^+) in the liquid electrolyte to reach zero at the electrode surface, assuming no convection.[51] Rosso *et al.* attributed the close agreement between the Sand time and the initiation of Li dendrites to non-uniformities in the concentration distribution, which they believed could be due to the SEI.[47] Nishikawa *et al.* concluded that depletion of Li^+ in the liquid electrolyte (due to diffusion limitations) is not a controlling factor for Li dendrite initiation, and that the dendrite initiation time is strongly correlated to the properties of the SEI layer.[52] Crowther and West also showed that the dendrite initiation time was independent of the liquid-phase mass transport properties.[49] These observations suggest that diffusion limitations within the SEI, rather than in the liquid electrolyte, could determine the Li dendrite onset time.

Solid-state diffusion is an important, rate-controlling process in many electro-chemical applications, including oxide film growth and fuel cells. Diffusion of Li^+ through the SEI was reviewed by Cheng *et al*.[6] Since Li^+ diffusion plays a key role in the electrochemical processes of SEI growth, one should expect it also to have a role in dendrite initiation. As outlined above, dendrites typically become favorable when approaching mass transport limitations. In the solid state, diffusion coefficients for Li^+ are in the range 10^{-10} to 10^{-9} cm^2 s^{-1} as provided in literature.[53,54] An analogous form of limiting current (Eq. 1.1) through the SEI can be estimated, assuming Li^+ diffusion is the limiting factor:

$$i_{\mathrm{L,SEI}} = \frac{nF\mathcal{D}_{\mathrm{SEI}}C_0}{L} \qquad [1.3]$$

Assuming the Li^+ concentration in the SEI C_0 is ~10^{-5} mol cm^{-3} (discussed later) and a typical SEI thickness L of 10 nm,[26] $i_{L,\mathrm{SEI}}$ is about 1 mA cm^{-2}, which is in the range of current densities that produce Li dendrites. Hence, solid-state diffusion can be a significant limitation to the availability of Li^+ within the SEI. Therefore, diffusion through the SEI is a key process for understanding the initiation and growth of dendrites during Li electrodeposition.

1.3 Importance of Temperature in Dendritic Lithium Electrodeposition

Low temperature charging shortens the cycle life of Li-ion and Li-metal batteries alike.[55-57] Li-ion batteries experience detrimental Li plating when charged at low temperatures.[58] The physical similarity of these two systems (*i.e.*, the presence of an SEI) and the related problems caused by sub-ambient temperature charging suggest an analogous transport limitation is at work.

The transport of Li^+ through the SEI is critical in determining the kinetics and stability of Li-metal in electrochemical systems.[26,59,60] Effects of temperature on Li battery performance and surface film growth were reported by Dey in the 1970s.[25] Churikov studied the role of temperature on charge-transfer kinetics at a Li electrode limited by transport processes within the SEI using pulse voltammetry,[61,62] as well as photoemission spectroscopy.[63] Despite intensive research activity characterizing and modeling the SEI,[53,54,64,65] the precise mechanism of Li^+ transport within the SEI is presently not well-understood.[66] Hess recently extended studies of the non-linearity in the SEI overpotential[67] to a wide temperature range for several alkali metal anodes, and found that conduction

mechanisms through SEI exhibit distinct temperature dependencies.[68] Shi *et al.* performed experimental and DFT simulation studies to investigate the hopping of Li^+ within the SEI, enabling the prediction of Li^+ diffusion coefficients and the Li^+ concentration evolution.[69] Benitez and Seminario carried out molecular dynamics simulations of Li^+ diffusional transport in the SEI in the temperature range 250–400 K.[70]

In relation to mechanisms of Li surface morphology evolution and dendrite formation, Mogi *et al.* studied the effect of temperature on SEI and Li deposition morphology using AFM.[71] While they found that the SEI became uniform and Li dendrites were suppressed at elevated temperatures, the uniform surface film formed at high temperatures did not prevent dendrite growth when plating was carried out at room temperature. This suggests that the effect of temperature on the SEI is reversible, so that high temperature cannot be used to form an inherently dendrite-mitigating SEI. Ota *et al.* also studied the correlation between Li surface film formation and plating morphology at various temperatures.[72] Using diffusion-reaction modeling,[19] Akolkar predicted a critical temperature below which uncontrolled Li dendrite propagation occurs.[73] This prediction was a consequence of increased mass transport resistance at low temperature and decreased reaction resistance provided by a thinner SEI. Love *et al.* performed experimental studies of dendrite initiation times at ambient and sub-ambient temperatures and observed an increase in the propensity for Li dendrites at low temperatures,[55] which was in qualitative agreement with the Akolkar model.[73] Hao *et al.* proposed that Li dendrites are initiated by two possible mechanisms: (i) Li^+ depletion at the Li-SEI interface, and (ii) non-uniformity of the SEI, causing non-uniform local deposition rates.[74] Recently, Mistry *et al.* presented a model of electrolyte confinement[75] to explain Li dendrite initiation beyond the Sand

criteria.[76] They also studied the effects of temperature on Li plating morphology. Sano *et al.* reported the effects of temperature on Li electrodeposition in an ionic liquid electrolyte.[77]

The studies mentioned above do not readily point to what temperature-dependent parameters are dominant in controlling the onset time of Li dendrites. While most of them refer to the SEI, its precise role in dendrite initiation and growth is yet unclear. A mechanistic model that closely agrees with experimental evidence and explains the effect of temperature on dendrite onset time is needed.

1.4 Objectives and Outline

Motivated by the gaps in current understanding outlined in sections 1.2 and 1.3, the specific objectives of the present research are:

1) Using experiments and mathematical modeling, to mechanistically understand the transport-reaction processes that lead to the formation of Li dendrites.
2) To understand the effects of various plating parameters (temperature, initial SEI thickness, and applied current density) on the onset time of Li dendrites.
3) Using modeling, to determine whether pulsed current is a practically advantageous strategy for suppressing Li dendrites during the recharge of Li metal batteries.

Chapters 2-4 address the above objectives. Chapter 5 provides a summary.

Chapter 2 investigates the fundamental problem of Li dendrite growth. Chronopotentiometry and optical imaging provide experimental observations for when dendrites first appear on a Li electrode. Electrochemical impedance spectroscopy (EIS) provides evidence for SEI growth and enables estimation of the SEI growth rates. These experiments guide the development of an analytical model that explains mechanistically what controls the onset time of dendrite growth during Li electrodeposition.

Chapter 3 discusses the effect of temperature on Li dendrite initiation. Chronopotentiometry and EIS are performed under controlled temperatures to study Li dendrite onset time and other effects of temperature. The observations are interpreted within the context of the analytical model (Developed in Chapter 2) in order to show what parameters are dominant in controlling dendrite onset time.

Chapter 4 shows a comparison between direct current (d.c.) and pulsed current (p.c.) Li electrodeposition. Numerical simulations of the Li^+ concentration profile within the SEI layer are used to make predictions of the dendrite onset time. Computations of the charge plated prior to the formation of dendrites enable a comparison of d.c. and p.c. at an equivalent Li-metal battery charging rate.

CHAPTER 2. Solid State Transport Limitations Explain the Onset Time of Dendritic Lithium Electrodeposition

Despite four decades of research on Li-metal batteries, rechargeable Li-metal anodes that do not evolve dendrites are still not commercially available.[7,14,78,79] In order to realize secondary Li-metal batteries, a comprehensive understanding of the Li dendrite initiation mechanism is required. In this chapter, the initiation of Li dendrites is investigated using electrochemical techniques and surface microscopy. The onset time of dendritic growth is explained in the context of diffusion limitations occuring within the solid electrolyte interphase.

The vast majority of studies of Li dendrite initiation, some of which were mentioned in Chapter 1, do not incorporate unsteady-state diffusional transport processes occurring within the SEI. For example, Wood *et al.* attempted, using experiments and computation, to identify a correlation between the Li surface morphology evolution and the heterogeneities in the surface SEI layer.[80] In their work, the non-uniform SEI thickness or composition manifests as variations in the Li deposition-dissolution kinetics, and this allowed predictive determination of voltage profiles during charge-discharge cycling of Li|Li symmetric cells.

It is shown in this chapter that solid-state transport effects are dominant in controlling the time when Li dendrites first form. A mathematical model is developed which incorporates the diffusional transport of Li^+ within the gradually thickening SEI. This model provides predictions of Li dendrite onset times which agree qualitatively with

several experimental observations. Finally, pulsed currents are shown to delay dendrite initiation, and this observation is explained in the framework of the transport model presented.

2.1 Experimental Procedure

2.1.1 Materials

A 0.38 mm thick Li ribbon (99.9%, Sigma-Aldrich) was used to prepare the working, counter, and reference electrodes. The electrodes were polished using 400 grit sanding sheets. Battery grade 1.0 M $LiPF_6$ solution in 1:1 (v/v) ethylene carbonate/dimethyl carbonate (EC/DMC, Sigma-Aldrich) electrolyte was used as received. Cylindrical cells were fabricated from PTFE[81] using a CNC router. A 0.127 mm thick Cu foil (99.9%, Alfa Aesar) was used as substrate for Li plating and subsequent anodic stripping coulometry.

2.1.2 Methods

Experiments were performed inside an Ar-purged glovebox (MBraun). Moisture inside the glovebox was maintained below 10 ppm. A 3-electrode configuration was employed in which the working and counter electrodes (WE, CE) were placed horizontally in the PTFE cell with an inter-electrode spacing of 2.5 cm (Fig. 2.1). A 2 mm diameter hole was drilled into the side of the PTFE cell approximately 1.5 cm away from the WE. A wedge-shaped Li foil, wrapped in PTFE tape to prevent leaking when fitted into this

hole, acted as the reference electrode (RE). The exposed portion of the WE was the same as the PTFE tube's inner diameter (1.8 cm). Thus, WE active surface area was 2.5 cm^2. The exterior portion of the WE was wrapped with PTFE tape and sealed using a PTFE cap as shown in Fig. 2.1. Electrical contact was made to the WE using a Cu wire current collector that was inserted through a hole drilled into the PTFE cap.

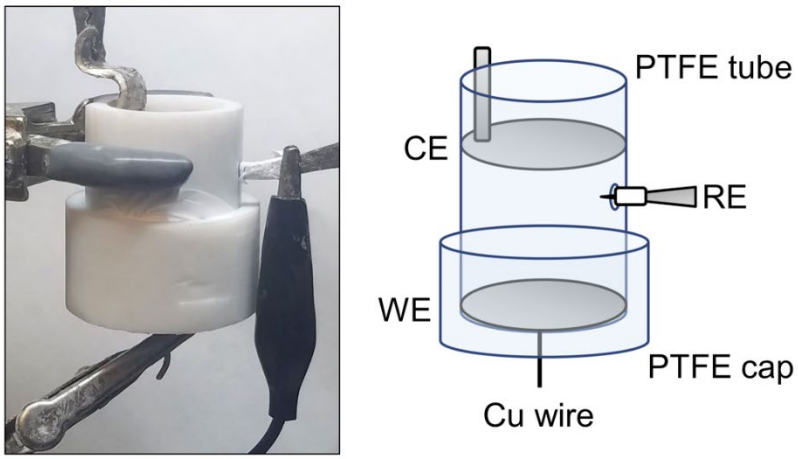

Figure 2.1 - Photograph (*left*) and schematic (*right*) of the PTFE cell setup used for Li electrodeposition studies and Li dendrite observations.

The Li WE was placed in the PTFE cell and was soaked in electrolyte (composition provided above) for various times (t_{soak}) between 1 min and 8 hr. Just before Li electrodeposition, additional electrolyte was added to the cell so as to make ionic contact between the WE and the CE. Between consecutive experiments, the WE and RE were not reused; however, the CE was reused after rinsing it with DMC solvent and allowing it to dry inside the glovebox. All electrochemical experiments were performed using a VersaSTAT 4 potentiostat/galvanostat with built-in frequency response analyzer

(Ametek). Chronopotentiometry was performed at various applied current densities, where current density (i) refers to the applied current normalized to the projected surface area of the WE. Galvanostatic plating was periodically halted and the CE was removed to optically image dendrites on the surface of the WE. In some cases, the electrolyte was poured out in order to improve optical image quality.

Electrochemical impedance spectroscopy (EIS) was used to monitor SEI growth. The direct current (d.c.) during EIS was 0 A and the RMS amplitude was 50 μA cm^{-2}. Linear polarization response to the EIS amplitude was confirmed in polarization experiments (Appendix A). A frequency range of 100 kHz to 1 Hz was used. A simple $R_{\mathrm{e}}(Q_{\mathrm{s}}R_{\mathrm{s}})$ equivalent circuit, where Q_{s} is a constant phase element (CPE), adequately fit the data over the frequency range studied. The ohmic resistance R_{e}, determined by EIS as the real impedance at high frequency, was used to correct for the iR drop in the liquid electrolyte. The surface resistance R_{s} was determined from the Nyquist impedance plot as discussed below. R_{s} provided an estimate of the SEI thickness.[26,82] Unlike ref. [82], SEI thickness was not estimated based on capacitance since the precise relationship between CPE parameters and the physical properties of the SEI layer was unavailable.[83]

Pulsed current (p.c.) Li electrodeposition was performed by applying i_{on}= 0.5 mA cm^{-2}, t_{on}= 0.7 ms and t_{off} = 3.3 ms. For Li electrodeposition using d.c. and p.c. waveforms, the Faradaic efficiency was measured via anodic stripping coulometry on Cu foil. Before Li plating, the Cu foil was cleaned in 2 M H_2SO_4 for 10 min, then rinsed with acetone and deionized water (Millipore). Li plating onto the Cu foil was performed in the PTFE cell described above.

2.2 Chronopotentiometry Studies of the Lithium Dendrite Onset Time

In this section, the Li dendrite onset time (τ_{onset}) during Li electrodeposition is investigated. Chronopotentiometry and optical imaging were used to study the initiation and growth of Li dendrites. After soaking a freshly polished Li WE in electrolyte (1 M $LiPF_6$ in 1:1 EC/DMC) for t_{soak} = 1 hr, galvanostatic plating at i = 0.5 mA cm^{-2} was performed for 1000 s in the PTFE cell described above. The electrode potential (V) was recorded and the surface overpotential η_s was calculated as:

$$\eta_s = V - iR_e \qquad [2.1]$$

where the ohmic resistance R_e is provided by EIS. Fig. 2.2 shows η_s (from Eq. 2.1) and the Li surface morphology (from optical microscopy) as a function of the Li plating time. The current densities used in these studies were well below the liquid phase mass transport limited current density, which is given by Eq. 1.1. Using values for $\mathcal{D}_{\text{liq}}$ and C_b of 10^{-5} cm^2 s^{-1} and 10^{-3} mol cm^{-3}, respectively, and assuming a natural convection boundary layer thickness δ of 0.01 cm, $i_L \cong 100$ mA cm^{-2}. Since $i \ll i_L$, this implies that liquid phase concentration overpotentials are negligibly small. For simplicity, we used the sign convention that cathodic (plating) current density and overpotential are positive quantities.

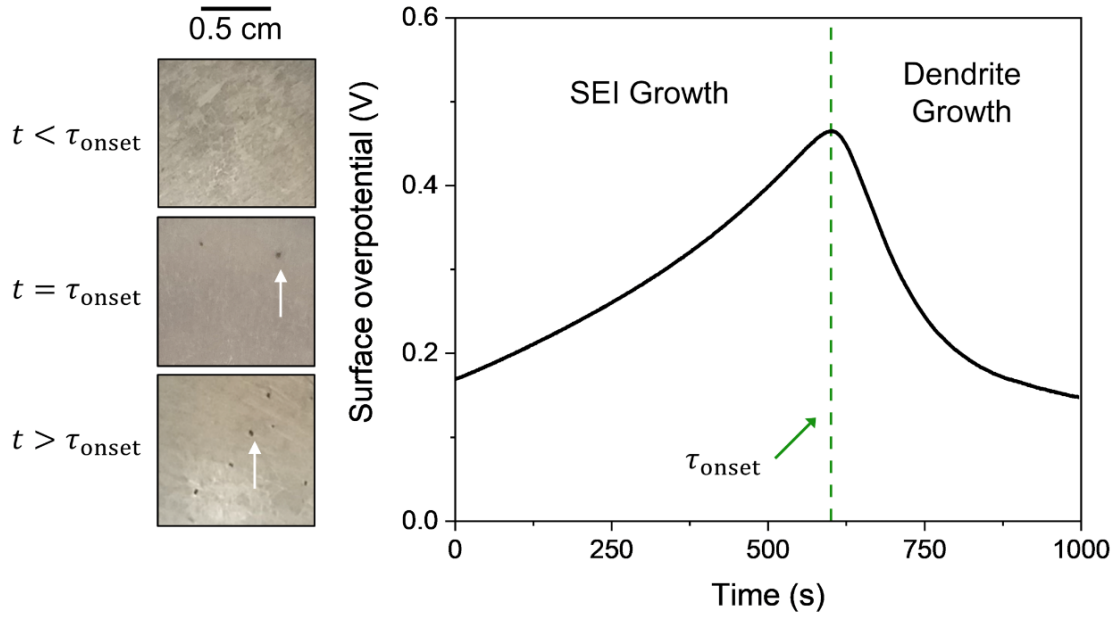

Figure 2.2 - Time-evolution of the surface overpotential (*right*) during galvanostatic Li electrodeposition at 0.5 mA cm^{-2} in 1 M $LiPF_6$ 1:1 EC/DMC. The Li foil electrode was soaked in the electrolyte for 1 hr before plating commenced. Photographs (*left*) of the Li metal surface at various time intervals during chronopotentiometry. At $t < \tau_{onset}$, no dendrites are observed. At $t = 600$ s (τ_{onset}), dendrites are first observed and this time coincides with the maximum in the surface overpotential. At $t > \tau_{onset}$, the surface gradually becomes depolarized as dendrites grow larger and their number increases.

In Fig. 2.2, a maximum in η_s is observed at $t \approx 600$ s. This time coincides with the first appearance of dendrites in optical microscopy observations of the Li WE (Fig. 2.2 *left*). Dendrite onset time (τ_{onset}) is defined as the time corresponding to the maximum in η_s and the time when dendrites first appear. Before η_s reached a maximum (*i.e.*, $t < \tau_{onset}$), no dendrites were observed. At times longer than τ_{onset}, dendrites increased in number and size as η_s gradually decreased. A temporal maximum in η_s was also noted in chronopotentiometry experiments at applied current densities of 0.1 and 2 mA cm^{-2} (Fig. 2.3) for t_{soak} = 1 hr. For these conditions too, optical microscopy confirmed that dendrites initiated at time $t = \tau_{onset}$ corresponding to the maximum in η_s. However, as noted in Fig.

2.3, τ_{onset} was lower (*i.e.*, earlier initiation of Li dendrites) when galvanostatic plating was performed at a higher current density. At 2 mA cm^{-2}, τ_{onset} was just 40 s (Fig. 2.3). At even higher currents (5 mA cm^{-2}, not shown in Fig. 2.3), dendrites initiated within the first seconds of plating.[80]

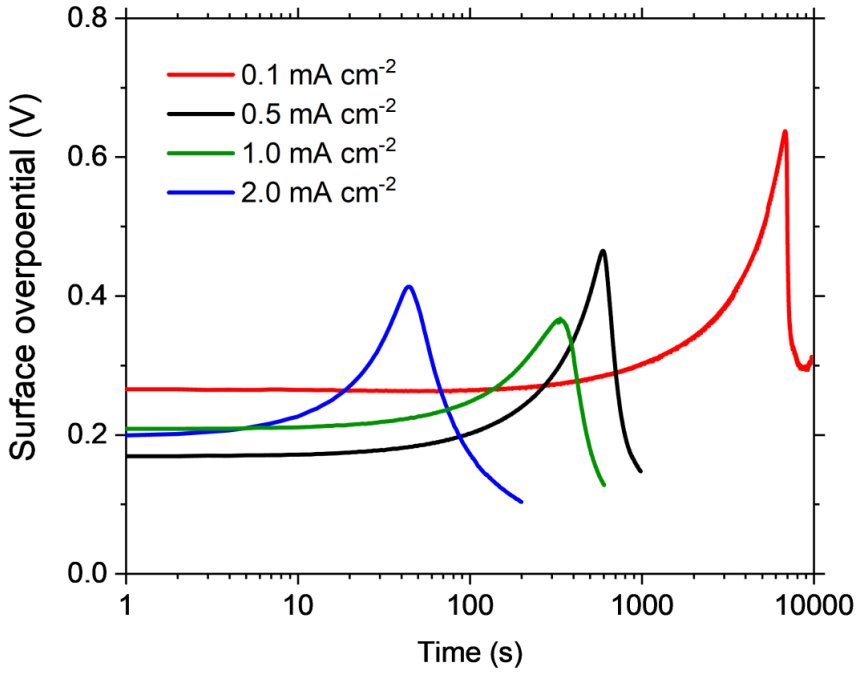

Figure 2.3 - Chronopotentiometry during Li electrodeposition performed at 2.0, 1.0, 0.5, and 0.1 mA cm^{-2} in 1 M $LiPF_6$ 1:1 EC/DMC. Soak time before plating was 1 hr. The onset time of dendritic Li electrodeposition, which coincides with the maximum in surface overpotential, decreases as the plating current density is increased.

2.3 Evidence of SEI Growth during Li Electrodeposition

During Li electrodeposition, the charge passed is utilized partly for SEI growth and partly for the plating of Li metal. SEI growth is a result of the precipitation of electrolyte reduction products, such as LiF, Li_2O, and Li_2CO_3.[28,84,85] Several cathodic reactions are in competition with the Li^+ reduction reaction in nonaqueous electrolytes, and these side reactions consume the active Li species, decreasing the useable capacity of the battery.[38,39,86-89] The irreversible capacity loss is evident based on coulombic efficiency measurements, shown later in this work (§2.5, §3.2.3).

The growth of the SEI layer on the Li WE manifests as a gradual increase in surface overpotential and surface resistance. Electrochemical impedance spectroscopy (EIS) was employed to characterize the surface changes during the various stages of Li electrodeposition. Nyquist plots obtained after Li electrodeposition ($i = 0.5$ mA cm^{-2}) for various time periods (0, 200, 400, 500 s) are shown in Fig. 2.4. In all cases, Li electrodeposition was preceded with soaking of the Li WE in aforementioned electrolyte for $t_{\mathrm{soak}} = 1$ hr. As seen in Fig. 2.4, the surface resistance R_{s} increased with Li plating time from 0 s to 400 s ($t = \tau_{\mathrm{onset}}$). However, prolonged Li plating beyond 400 s ($t > \tau_{\mathrm{onset}}$) lowered considerably the value of R_{s}. Note that τ_{onset} corresponding to the data in Fig. 2.4 is somewhat lower than that in Fig. 2.2. This is due to the run-to-run variability in chronopotentiometry data, which yielded a coefficient of variation of about 40%, as will be discussed below. Much of the run-to-run variability was due to temperature variation, which was controlled in the experiments of Chapter 3.

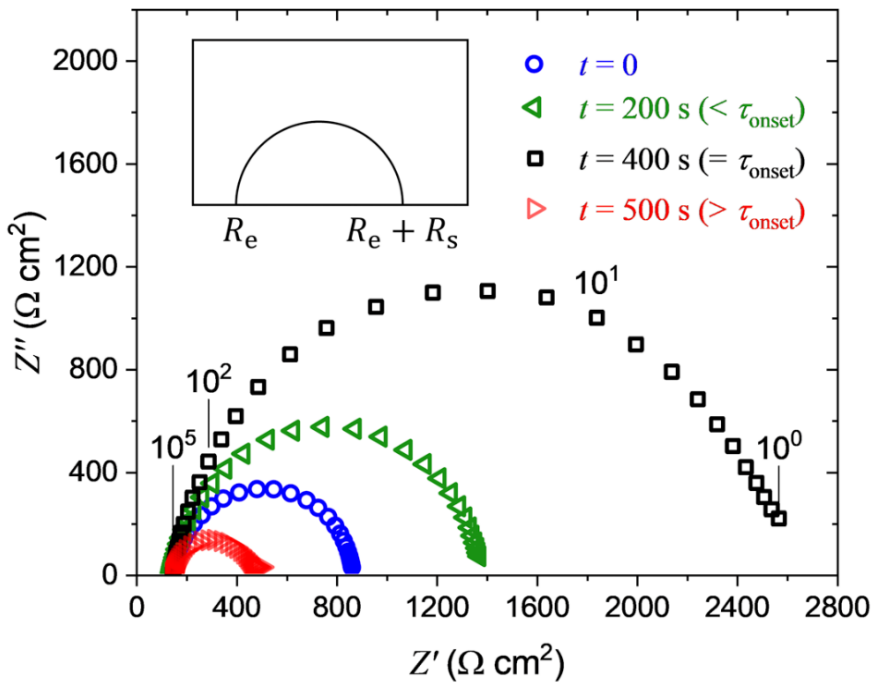

Figure 2.4 - Nyquist plots after various time intervals (0, 200, 400 and 500 s) of Li electrodeposition at 0.5 mA cm^{-2} in 1 M $LiPF_6$ 1:1 EC/DMC. The soak time before electrodeposition was 1 hr. During EIS, the direct current (d.c.) was set at 0 A and the RMS amplitude was 50 μA cm^{-2}. Select frequencies from 100 kHz to 1 Hz are labeled above the data for $t = \tau_{\text{onset}}$.

During Li plating, the electrolyte ohmic resistance R_e is observed to remain constant. For Li plating time periods $t < \tau_{\text{onset}}$, R_s was observed to increase linearly with t as shown in Fig. 2.5 at applied current densities of 0.5, 1 and 2.0 mA cm^{-2}. Run-to-run variability is also present in the measurements of SEI growth rates, which explains the

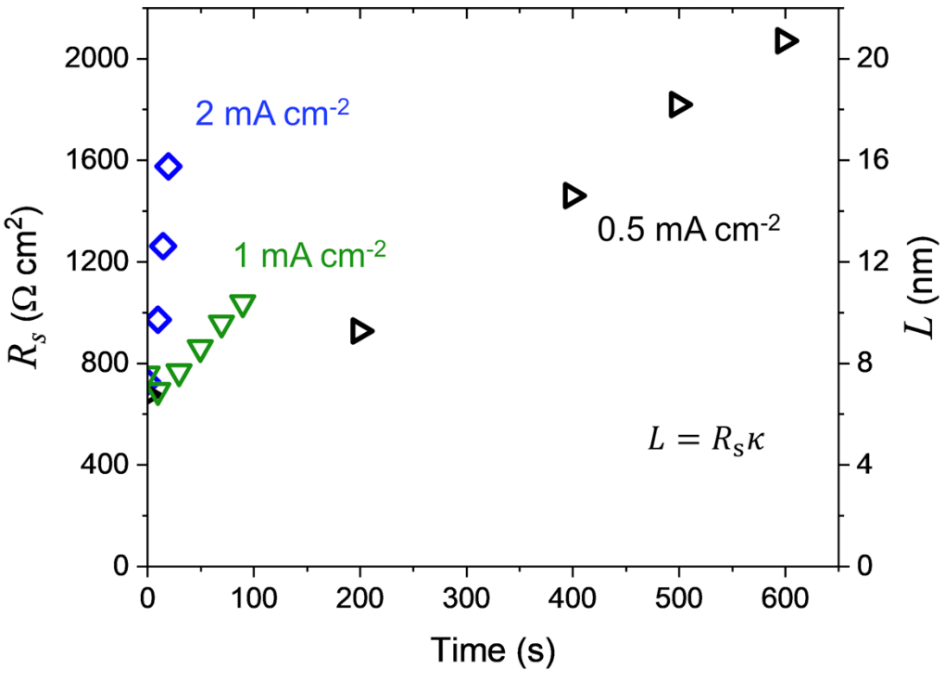

Figure 2.5 - Surface resistance (R_s) and apparent SEI thickness (L) as a function of plating time at current densities of 2.0, 1.0, and 0.5 mA cm^{-2}. The calculation of L is based on the SEI model: $L = R_s\kappa$, where the ionic conductivity κ was taken as 10^{-9} S cm^{-1}, representative of Li_2CO_3.[82]

difference between R_s values in Fig. 2.4 and 2.5 measured at 0.5 mA cm^{-2}. The apparent thickness of the SEI layer (L) can be determined from R_s using the SEI model:[26,82]

$$L = \kappa R_s \qquad [2.3]$$

where κ is the ionic conductivity of the SEI. In our work, κ was taken as 10^{-9} S cm^{-1}, representative of the ionic conductivity of Li_2CO_3.[82] Since L is proportional to R_s and since R_s increases linearly with t, our results suggest a relatively time-invariant SEI growth rate as seen in Fig. 2.5. Estimated SEI thickness values (from Eq. 2.3) are shown in Fig. 2.5 (secondary axis). It is also observed that the SEI growth rate depends on the applied current.

At higher currents, the SEI was observed to grow faster. It is noteworthy that as i increases from 0.5 to 1.0 mA cm^{-2}, the SEI growth rate as indicated by R_s roughly doubles.

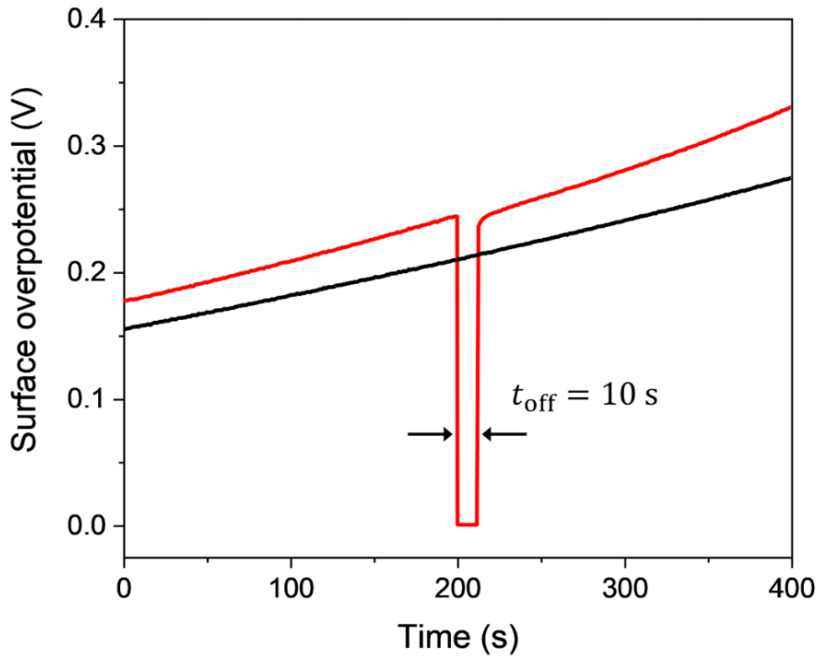

Figure 2.6 - Chronopotentiometry during Li electrodeposition at 0.5 mA cm^{-2} after 1 hr soak in 1 M $LiPF_6$ with current interruption (*red*) and without interruption (*black*).

Further evidence of SEI growth prior to the onset of dendrites ($t < \tau_{onset}$) during Li electrodeposition is provided by current interruption studies (Fig. 2.6). In these studies, Li plating (0.5 mA cm^{-2}) was temporarily interrupted by turning the current off (for a time period t_{off} = 10 s) and the response of the surface overpotential η_s was monitored. Since relaxation of the Li^+ concentration gradient within the liquid electrolyte occurs within 10 s ($= \delta^2/\mathcal{D}_{liq}$ where $\delta \sim 0.01$ cm and $\mathcal{D}_{liq} \sim 10^{-5}$ cm^2 s^{-1}), the 'off' period of 10 s should allow enough time for concentration polarization effects to decay completely. Accordingly, in the absence of concentration polarization, the return of the surface overpotential η_s (Fig.

2.6) back to nearly the same value as it was before applying the current interruption indicates that the surface resistance is attributable to a 'permanent' change in the electrode surface during Li plating, *i.e.*, growth of SEI layer. The SEI layer controls the surface resistance R_s and potential η_s during Li plating.

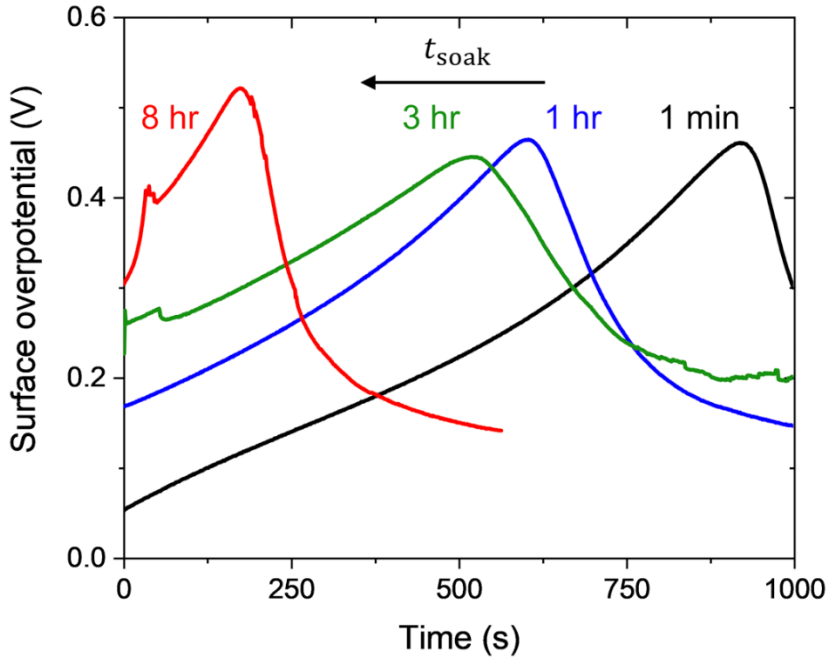

Figure 2.7 - Chronopotentiometry during Li electrodeposition at 0.5 mA cm^{-2} after 1 min (*black*), 1 hr (*blue*), 3 hr (*green*), and 8 hr (*red*) soak in 1 M $LiPF_6$ 1:1 EC/DMC. The onset time of dendritic Li electrodeposition decreases as the soak time increases. Additionally, the initial ($t = 0$) surface overpotential increases with increasing t_{soak}.

It is noteworthy that τ_{onset} is also a function of the time period for which the Li WE is soaked in electrolyte (t_{soak}) before Li electrodeposition is performed. Chronopotentiometry data for t_{soak} ranging from 1 min to 8 hr is shown in Fig. 2.7. During the soak time, SEI grows on the Li WE surface due to reduction of electrolyte components.[26] The SEI growth manifests as two effects which can be readily observed in

chronopotentiometry: (i) the initial η_s, *i.e.*, at $t = 0$, increases with t_{soak}, indicating a thicker SEI before Li plating begins; and (ii) τ_{onset} (when η_s reaches a maximum) decreases with t_{soak}, suggesting that Li dendrites initiate earlier on an electrode surface already covered with a thicker SEI layer. The latter effect will be analyzed in more detail in the following section.

Figs. 2.4–7 and the related discussion establish that at $t < \tau_{onset}$ the surface potential η_s gradually increases on account of SEI growth; thus, this phase is termed the 'SEI Growth' phase in Fig. 2.2. At longer times, *i.e.*, $t > \tau_{onset}$, dendrites are observed on the Li electrode together with electrode depolarization and thus we term this phase the 'Dendrite Growth' phase. In the context of these two phases, τ_{onset} may be viewed as the time at which Li electrodeposition transitions from the 'SEI Growth' phase to the 'Dendrite Growth' phase.

2.4 Transport Model for Prediction of the Dendrite Onset Time

In this section, a mathematical model is developed for characterization of the Li dendrite onset time (τ_{onset}) and its dependence on the Li plating current density. The model is based on considerations of Li^+ diffusion through a temporally evolving SEI layer on the Li surface. During Li electrodeposition, the Li surface is transformed gradually as shown in Fig. 2.8 and discussed below.

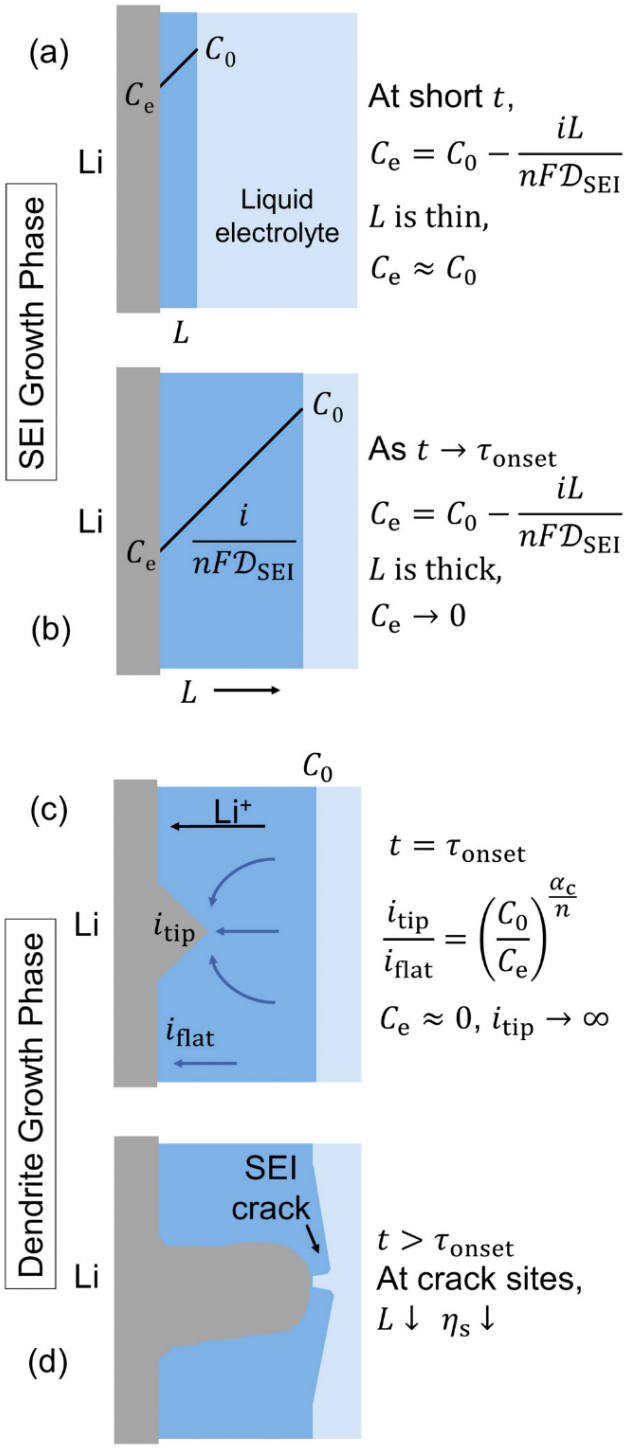

Figure 2.8 - Schematic showing a Li electrode submerged in liquid electrolyte and covered with SEI of thickness L: (a) During galvanostatic electrodeposition, a linear Li^+ concentration gradient develops across L. (b) After continued electrodeposition, the SEI grows thicker and the concentration of Li^+ at the electrode surface C_e decreases, eventually approaching zero. (c) The Li^+ concentration depletion near the Li–SEI interface promotes dendrite initiation. (d) Dendrites rupture the SEI so that accelerated Li plating is concentrated where the SEI is thin or absent.

2.4.1 'SEI-Growth' Phase

A Li electrode in contact with organic electrolyte is initially covered with a thin SEI layer (thickness L) as shown schematically in Fig. 2.8a. Upon application of a fixed current (of magnitude i), a linear concentration profile of Li^+ ions is established across the SEI layer. Establishment of the linear concentration profile is rapid with a short time constant ($t_{\text{diff}} = L^2/\mathcal{D}_{\text{SEI}}$ = 1 ms assuming L ~ 10 nm and $\mathcal{D}_{\text{SEI}}$ ~ 10^{-9} cm^2 s^{-1}). The concentration C_e of Li^+ at the Li–SEI interface is given by:

$$C_e = C_0 - \frac{iL}{nF\mathcal{D}_{\text{SEI}}} \qquad [2.4]$$

where $\mathcal{D}_{\text{SEI}}$ is the Li^+ diffusion coefficient in the SEI. As stated above, $\mathcal{D}_{\text{SEI}}$ was taken as 10^{-9} cm^2 s^{-1}. This value is within the general range of diffusivities for Li^+ in Li_2CO_3.[54] The bulk concentration C_0 of mobile Li^+ ions in Li_2CO_3 was assumed to be ~10^{-5} mol cm^{-3} at 25 °C.[54] Eq. 2.4 indicates that, as time increases and the SEI grows thicker, the Li^+ concentration at the Li–SEI interface decreases. When the SEI thickness approaches $L = nF\mathcal{D}_{\text{SEI}}C_0 i^{-1}$, the interfacial Li^+ concentration C_e approaches zero (Fig. 2.8b). This condition makes the Li electrode prone to dendrite formation as discussed in (*b*) below. The steady growth of the SEI layer during the 'SEI Growth' phase manifests as a steady increase in the surface resistance R_s and thus the overpotential η_s.

2.4.2 Lithium Dendrite Initiation

Towards the end of the 'SEI Growth' phase, the Li–SEI interface experiences depletion of the Li^+ ion concentration: $C_e \rightarrow 0$. Under such depleted conditions, surface roughness on the electrode is amplified during Li electrodeposition as depicted in Fig. 2.8c. The preferential Li deposition on the tip of a surface asperity is due to the fact that micro-scale surface roughness elements are released from mass transport limitations,[16] as a result of enhanced spherical diffusion of Li^+ ions to the tip. On the other hand, the Li deposition onto the surrounding 'flat' electrode experiences Li^+ diffusion limitations. Through considerations of the rate-limiting processes on a dendrite tip (*i.e.*, electrochemical kinetics) and those on the 'flat' electrode (*i.e.*, diffusional transport), Banik[90] and Akolkar[19] previously derived a simple equation for the ratio of the dendrite tip current density (i_{tip}) to the 'flat' electrode current density (i_{flat}):

$$\frac{i_{tip}}{i_{flat}} = \left(\frac{C_0}{C_e}\right)^{\frac{\alpha_c}{n}} \qquad [2.5]$$

where n = 1 for Li^+ and α_c is the cathodic charge transfer coefficient for Li electrodeposition which ranges from 0.2 to 2.0.[91] In our work, we selected α_c = 0.4 to be consistent with the majority of literature reports.[19,49] Eq. 2.5 indicates that as $C_e \rightarrow 0$, the ratio of dendrite tip to flat surface current densities (i_{tip}/i_{flat}) approaches infinity, *i.e.*, a condition which makes the Li electrode surface prone to dendrite formation at time $t = \tau_{onset}$.

2.4.3 'Dendrite Growth' Phase

The growing dendrites eventually rupture the SEI layer, exposing active Li metal at the dendrite tip to the electrolyte (Fig. 2.8d).[39] Li electrodeposition at the active Li metal surface causes depolarization (η_s is lowered) because the SEI layer at the exposed dendrite tip is either very thin or completely absent. This is supported by polarization studies of Li electrodeposition as a function of the SEI thickness, which show that Li electrodeposition is kinetically accelerated (*i.e.*, increased apparent exchange current density for Li deposition) when the SEI is thin (Appendix A).

2.4.4 Analytical Model for Prediction of Li Dendrite Onset Time

An analytical solution for the dendrite onset time τ_{onset} follows from the processes described above. By combining Eq. 2.4 and Eq. 2.5, we obtain a relationship between the dendrite-to-flat current density ratio ($i_{\text{tip}}/i_{\text{flat}}$) and the SEI thickness (L):

$$L = \frac{nF\mathcal{D}_{\text{SEI}}C_0}{i}\left[1 - \left(\frac{i_{\text{flat}}}{i_{\text{tip}}}\right)^{\frac{n}{\alpha_c}}\right] \qquad [2.6]$$

At $t = \tau_{\text{onset}}$, $i_{\text{tip}}/i_{\text{flat}} \to \infty$ or $i_{\text{flat}}/i_{\text{tip}} \to 0$. Thus, at $t = \tau_{\text{onset}}$, Eq. 2.6 is simplified and provides a value for the critical SEI thickness (L_{onset}) at which dendritic growth becomes favorable due to Li^+ mass transport limitations:

$$L_{\text{onset}} = \frac{nF\mathcal{D}_{\text{SEI}}C_0}{i} \qquad [2.7]$$

Note that $\mathcal{D}_{\mathrm{SEI}}$ and C_0 refer to properties of the SEI layer. We determined that the SEI thickness L is approximately a linear function of the plating time t (as seen in Fig. 2.5):

$$L = L_0 + \dot{L}t \qquad [2.8]$$

where $\dot{L}$ is the SEI growth rate and L_0 is the initial ($t = 0$) SEI thickness which depends on t_{soak}. Thus, the time τ_{onset} when $L = L_{\mathrm{onset}}$ is found by substituting Eq. 2.8 into Eq. 2.7:

$$\tau_{\mathrm{onset}} = \frac{1}{\dot{L}}\left(\frac{nF\mathcal{D}_{\mathrm{SEI}}C_0}{i} - L_0\right) \qquad [2.9]$$

Eq. 2.9 represents the Li dendrite onset time as a function of the physicochemical and transport properties of the SEI ($\mathcal{D}_{\mathrm{SEI}}$ and C_0) as well as the SEI thickness L, approximated as a linear function of plating time with parameters (L_0, $\dot{L}$) determined by EIS measurements. Estimated values for the parameters such as $\mathcal{D}_{\mathrm{SEI}}$, C_0, and κ in Eq. 2.9 are available in literature, although their accuracy and dependence on other factors (such as electrolyte composition) is unknown. Eq. 2.9 predicts that τ_{onset} decreases as i increases, which is consistent with experimental data in Fig. 2.3. Eq. 2.9 also predicts that τ_{onset} decreases as the soak time increases (*i.e.*, greater L_0), which is qualitatively consistent with data in Fig. 2.7.

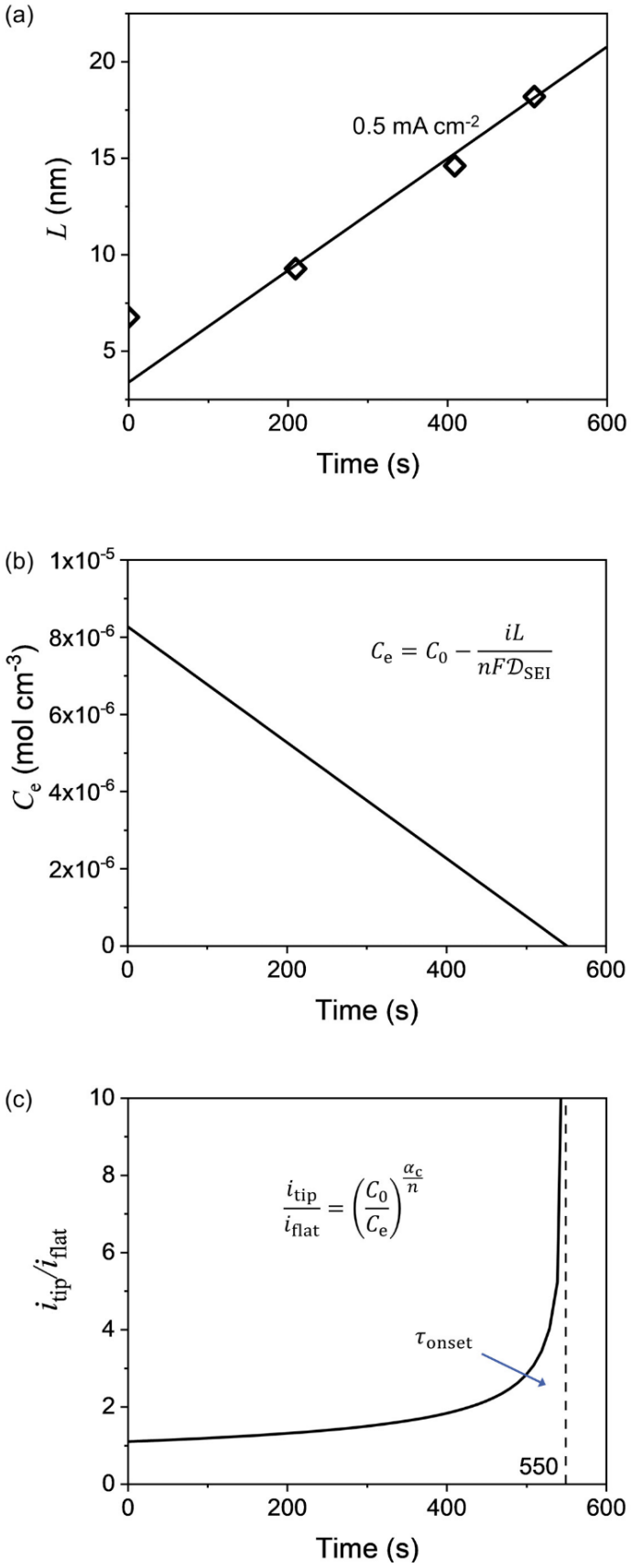

Figure 2.9 - Model prediction of τ_{onset} at Li plating current density 0.5 mA cm^{-2} is shown: (a) The SEI thickness grows linearly with time (per Fig. 5); (b) C_e decreases as L increases per Eq. 3; (c) When C_e approaches 0, the ratio $i_{\text{tip}}/i_{\text{flat}}$ increases dramatically. The time when this occurs is the onset time (*dashed line*) of Li dendrites.

Fig. 2.9 shows the process used for computing τ_{onset} for 0.5 mA cm^{-2}. A linear fit to the SEI thickness vs. time curve obtained from EIS (Fig. 2.9a) provides L_0 and $\dot{L}$. Knowing the time-dependent SEI thickness (L), the interfacial Li^+ concentration C_e was calculated using Eq. 2.3 (Fig. 2.9b). Finally, in Fig. 2.9c $i_{\text{tip}}/i_{\text{flat}}$ was computed by applying Eq. 2.6, and τ_{onset} was determined using Eq. 2.9. At 0.5 mA cm^{-2}, this predicted τ_{onset} was determined to be 550 s, which is within the spread of experimentally determined τ_{onset} values shown in Fig. 2.10.

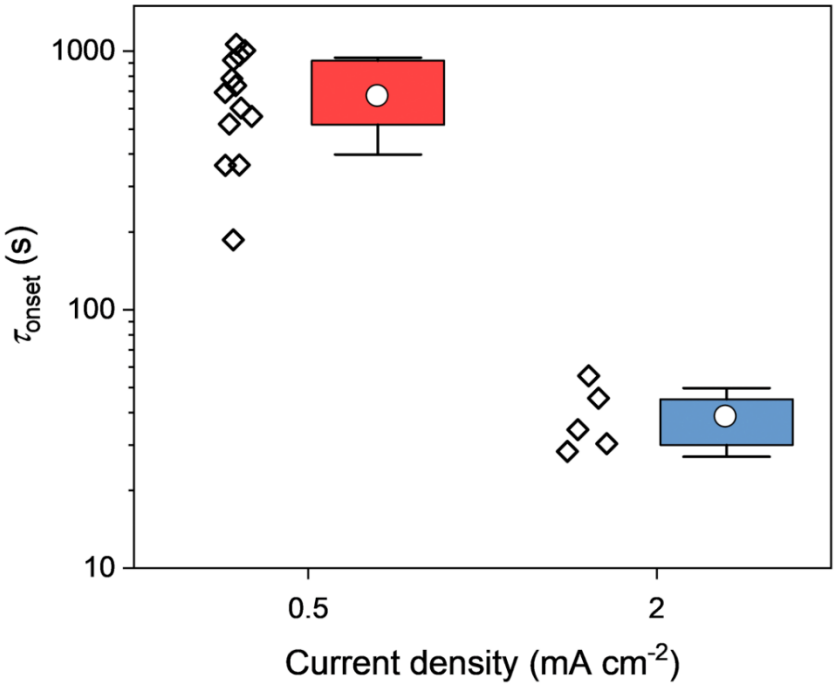

Figure 2.10 - Dendrite onset times measured in experiments at 0.5 and 2.0 mA cm^{-2}. Scattered diamonds indicate experimental data, whiskers represent 1 standard deviation, the colored bar indicates the interquartile range, and white circles indicate mean values.

At a higher current density of 2.0 mA cm^{-2}, $\dot{L}$ is roughly 10 times larger than at 0.5 mA cm^{-2}. This implies that τ_{onset} at 2.0 mA cm^{-2} should be roughly one fortieth of that at

0.5 mA cm^{-2}, *i.e.*, τ_{onset} is of the order of magnitude of 10 s. This order of magnitude estimate is also consistent with the experimentally observed τ_{onset} for 2.0 mA cm^{-2} of ~30 s shown in Fig. 2.10. The variability in measurement of $\dot{L}$ based on EIS and the uncertainty in the values of $\mathcal{D}_{\text{SEI}}$, C_0, and κ prohibit a more quantitative comparison between the model and experiments. However, the qualitative agreement is favorable. Another qualitative prediction consistent with experiment is the dependence of τ_{onset} on soak time, *i.e.*, greater soak time yields greater L_0, and thus, shorter τ_{onset}. This prediction is consistent with the observations in Fig. 2.7. The qualitative agreement between experiments and the model predictions establishes confidence that the model captures the essential features of the transport phenomena leading to the onset of Li dendrites.

2.5 Experimental Studies of Pulsed Current Electrodeposition

It is clear from the above discussion that Li^+ transport limitations associated with a temporally evolving SEI are crucial in determining the onset time of dendrites. The aim in this section is to demonstrate how pulsed current (p.c.) may be used to mitigate Li^+ concentration depletion within the SEI. By providing short time periods when the current is turned off, Li^+ concentration gradients developed in the SEI during the 'on' period can be relaxed, delaying dendrite initiation. The time period for which the current should be turned off (t_{off}) was selected based on guidance from the transport model developed above. When the current is turned off, diffusion is the predominant mode of transport which replenishes the Li^+ in the SEI and nullifies the concentration gradient across the SEI. As discussed above, the diffusion time constant $t_{\text{diff}} = L^2/\mathcal{D}_{\text{SEI}}$ has a value of ~1 ms for a 10

nm thick SEI. Thus, the Li^+ concentration gradient that develops across the SEI can be nullified in ~1 ms. To provide a safety margin, especially given the variability in the SEI thickness, we chose t_{off} = 3.3 ms. The pulse 'on' time was set at t_{on} = 0.7 ms (Fig. 2.11 *right*) and the instantaneous 'on' current was set at 0.5 mA cm^{-2} in order to match the d.c. applied current density. The time t_{on} was chosen to be smaller than t_{diff} of 1 ms to avoid substantial Li^+ depletion within the SEI. Thus, the chosen p.c. waveform represents a time-averaged reaction current that is lower than d.c., implying a slower charging rate of a Li-metal battery. While this is undesirable for practical applications, the purpose behind selecting above p.c. parameters is to demonstrate that p.c. mitigates Li^+ concentration depletion effects within the SEI and delays dendrite formation. Further, matching i_{on} to i used in d.c. maintains the same concentration gradient and roughly the same SEI growth rate during the 'on' period. Equivalent d.c. and p.c. charging rates are compared in Chapter 4 via COMSOL® simulations of diffusional transport within the SEI.

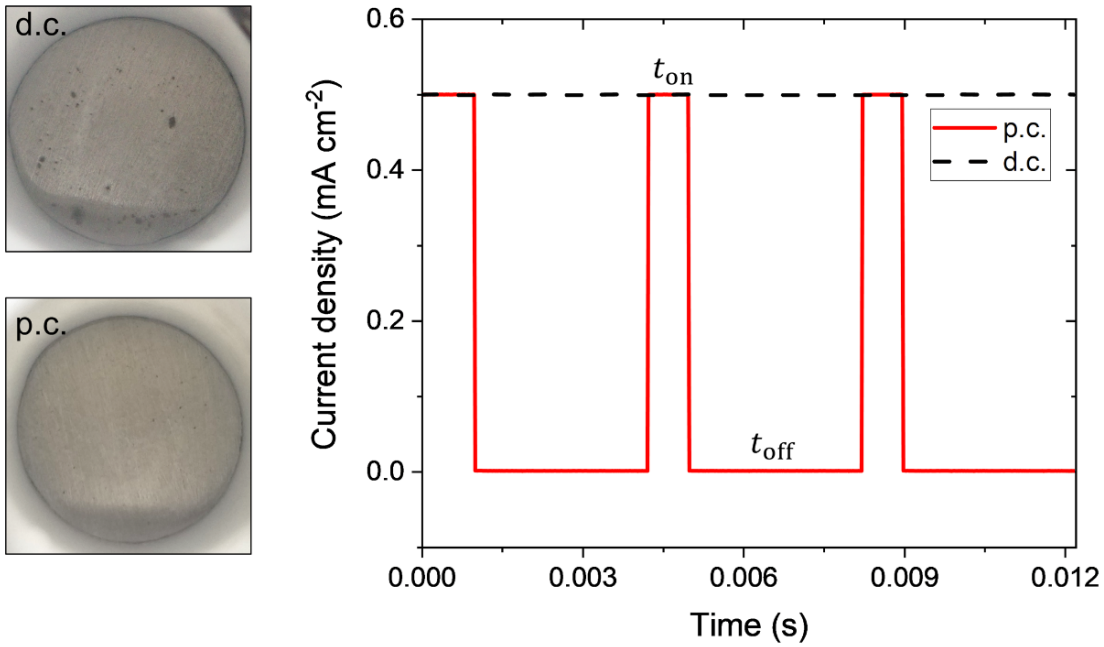

Figure 2.11 - The d.c. and p.c. waveforms (*right*) used to compare surface morphology of Li electrodeposits (*left*). Deposition was performed for the same net charge passed (1.63 C). Electrolyte was 1 M $LiPF_6$ 1:1 EC/DMC.

Fig. 2.11 *left* shows optical images of a Li WE after d.c. (*top*) and p.c. (*bottom*) plating. Since p.c. exhibited a lower coulombic efficiency (ε) compared to d.c. ($\varepsilon_{p.c.} = 42\%$ and $\varepsilon_{d.c.} = 67\%$, Fig. 2.12), the total duration of p.c. was prolonged so that 1.63 C equivalent of Li was plated both under d.c. and p.c. conditions. This corresponds to a Li deposit thickness of roughly 0.86 µm. As seen in the optical images (Fig. 2.11 *left*), p.c. provided a smooth Li deposit surface appearance whereas d.c. led to the growth of 3–4 large dendrites each ~0.1 cm in size. These observations of a smoother deposit in p.c. plating of Li are consistent with the simulation results of Mayers *et al.*[92] and with the experimental findings of Yang *et al.*[93] However, it should be emphasized that, although the charge of deposited Li was equivalent, the plating rate for the p.c. condition was lower than d.c.

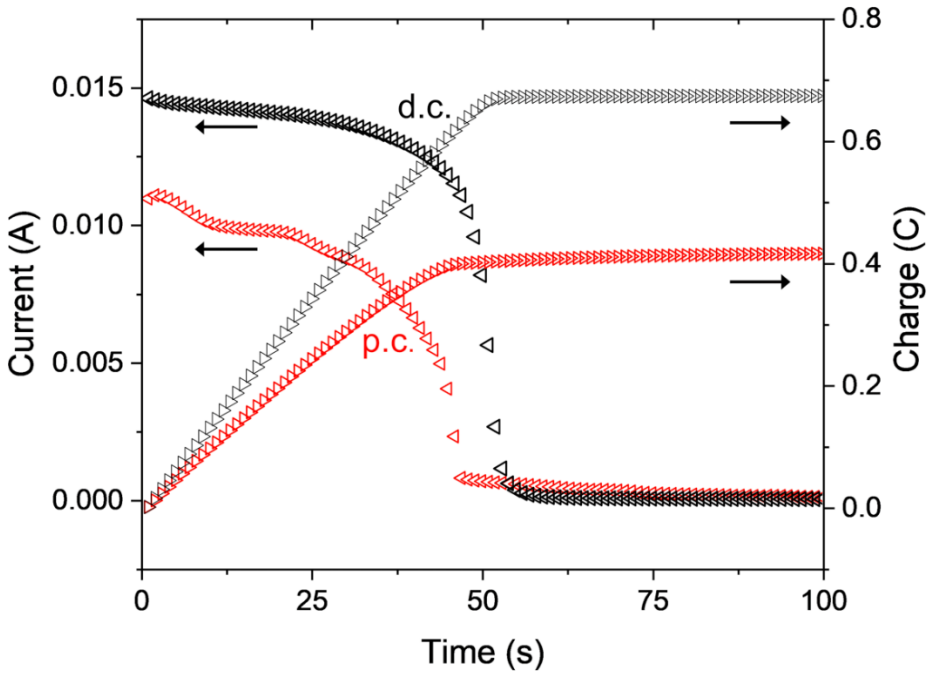

Figure 2.12 - Stripping coulometry of Li on Cu substrate performed at 1 V vs. Li/Li^+ after electrodeposition of 1.02 C by d.c. (*black*) and p.c. (*red*) at 0.5 mA cm^{-2}. The coulombic efficiency of p.c. ($\varepsilon_{p.c.}$) was 42% while the $\varepsilon_{d.c.}$ was 67%.

EIS was used to measure R_s and L during p.c. as a function of time (Fig. 2.13). The SEI growth rate ($\dot{L}$) during p.c. was found to be roughly the same as that during d.c. plating initially (*i.e.*, $t < \tau_{onset}$). However, at longer times, R_s and thus L continued increasing during p.c., whereas R_s decreased during d.c. plating when t exceeded τ_{onset} (shown earlier in Fig. 2.4). The drop in R_s for $t > \tau_{onset}$ in d.c. plating, which is an indirect indicator of dendrite formation, was absent for p.c. plating. Therefore, the proper application of p.c. (short t_{on} and $t_{off} > t_{diff}$) may enable relaxation of Li^+ concentration gradient within the SEI, which in turn mitigates the key condition ($C_e \rightarrow 0$) responsible for dendrite initiation. The successful mitigation of concentration depletion prevents SEI rupture, thereby promoting smoother Li deposits.

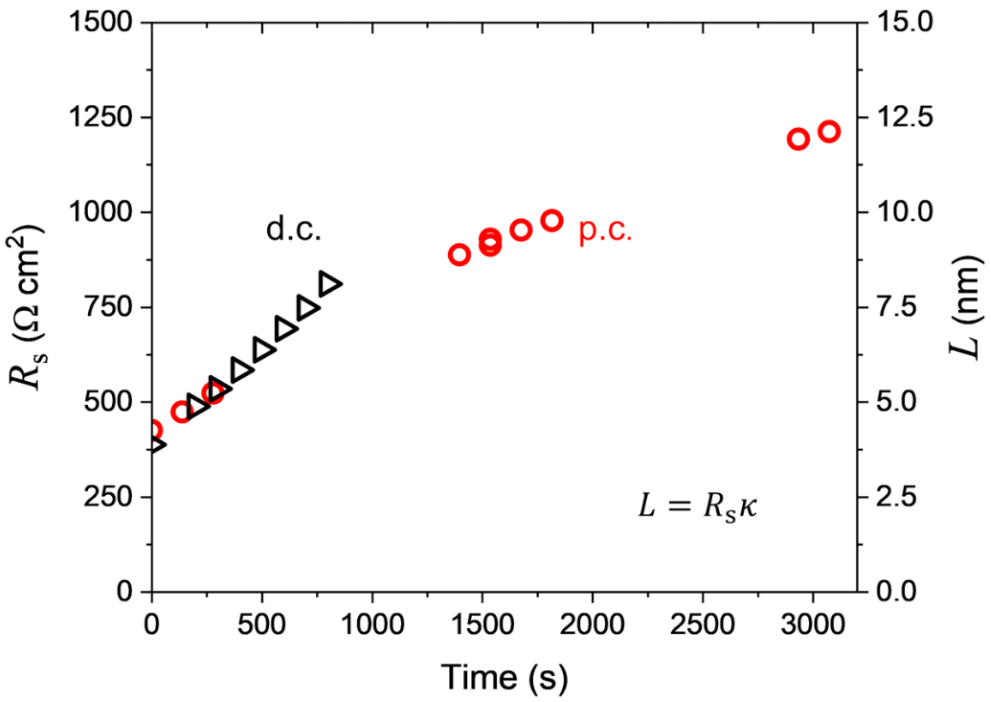

Figure 2.13 - Surface resistance (R_s) and apparent SEI thickness (L) as a function of plating time for d.c. (*black* triangles) and p.c. (*red* circles) waveforms shown in Fig. 2.11. In the p.c. data, plating time only includes the time when current is on.

The pulsing studies reported in this chapter support the mechanistic model of Li dendrite initiation due to Li^+ transport limitations within a temporally evolving SEI layer and provide some guidance for designing pulsing waveforms that could mitigate dendrites during Li electrodeposition. Chapter 4 will provide more detailed analysis of pulsing at an equivalent Li plating rate via numerical simulations.

2.6 Conclusions

The time when dendrites initiate during Li electrodeposition was investigated using experiments and modeling. The following key conclusions can be drawn from the results presented in this chapter:

(i) The onset of Li dendrite growth occurs at a time ($t = \tau_{\text{onset}}$) when the surface overpotential during galvanostatic Li electrodeposition exhibits a maximum. An 'SEI Growth' phase ($t < \tau_{\text{onset}}$) followed by a 'Dendrite Growth' phase ($t > \tau_{\text{onset}}$) were identified.

(ii) During the 'SEI Growth' phase ($t < \tau_{\text{onset}}$), the SEI layer on the Li surface gradually thickens. This is manifest through the increase in surface overpotential and surface resistance.

(iii) At $t = \tau_{\text{onset}}$, the Li^+ concentration at the Li–SEI interface reaches zero. The concentration depletion promotes dendrite formation because micro-scale surface roughness elements are free from transport limitations and are thus amplified into dendrites.

(iv) During the subsequent 'Dendrite Growth' phase ($t > \tau_{\text{onset}}$), the SEI layer is ruptured by the growing dendrites. This causes surface depolarization because the Li plating on essentially SEI-free dendrites exhibits fast kinetics.

(v) Using an analytical transport model, an equation predicting τ_{onset} (Eq. 2.8) was developed. Values for τ_{onset} determined using Eq. 2.8 were found to be in qualitative agreement with experimental results.

(vi) Pulsed current (p.c.) plating was investigated for its potential to suppress Li dendrite growth. Analysis of p.c. plating supports the mechanistic model that Li

dendrites initiate due to Li^+ transport limitations within a gradually thickening SEI layer.

The conclusions stated above highlight the interaction between physical properties of the SEI and operating conditions. These conclusions also motivate investigations of the effect temperature on the thickness, growth rate, and transport properties of the SEI layer, as will be discussed in Chapter 3.

CHAPTER 3. Temperature Dependence of Lithium Electrodeposition

Meeting the demand for high-energy density 'beyond Li-ion' batteries remains a challenge due to the rapid capacity fade and safety concerns of secondary Li-metal anodes.[4,7,94,95] The key bottleneck in developing rechargeable Li-metal anodes is the uneven or dendritic morphology evolution during battery charging.[6,9,96] Whereas a number of studies have attributed the initiation of dendrites to non-uniformities in the solid electrolyte interphase (SEI),[13,35,37,39,47,80,97,98] the previous chapter demonstrates the critical role of Li^+ transport through a gradually thickening SEI. Specifically, the model incorporates Li^+ transport limitations in the SEI and explains the influence of important factors on the dendrite initiation time, including the Li plating current density, the initial SEI thickness, and the application of pulsed currents.

In this chapter, the effect of temperature on the dendrite initiation time is explained in the context of the mechanistic model developed in Chapter 2. Electrochemical measurements of the dendrite onset time are shown to be a function of temperature. Chronopotentiometry and optical imaging are used to quantify the time at which Li dendrites initiate. This initiation occurs at a temporal maximum in the surface overpotential – a unique electrochemical signature that corresponds with, and thus helps easily identify, the first morphological appearance of Li dendrites. Electrochemical impedance spectroscopy (EIS) is used to measure the growth of the SEI before and during Li electrodeposition over a range of temperatures. The continuous growth of the SEI leading to the depletion of Li^+ at the Li-SEI interface during electrodeposition, and the

consequential onset of Li dendritic growth, are considered. The diffusional transport of Li^+ through the SEI is shown to be the critical temperature-dependent process that explains the rapid initiation of Li dendrites at sub-ambient temperatures.

3.1 Experimental Procedure

3.1.1 Materials and Cell Construction

Li ribbon (99.9%, Sigma-Aldrich) with 0.38 mm thickness was used to prepare the working (WE), counter (CE), and reference (RE) electrodes. The electrode surfaces were polished with 400 grit sanding sheets. Discs were cut from the Li ribbon using a 0.5" diameter punch. Chemical-resistant compression tee fittings for 0.5" OD plastic tubing were used to construct the electrochemical cells (McMaster Carr). Stainless steel rod 0.5" in diameter was inserted into the compression fittings, sealing the Li WE and CE in place (Fig. 3.1). The projected area of the exposed Li WE and CE was 0.672 cm^2. A length of 18-gauge copper wire, which was used to contact the RE, was guided through the PTFE stopper inserted into the top of the tee fitting. The tip of the wedge-shaped Li RE exposed to electrolyte was cleaved prior to each experiment. Battery grade 1.0 M $LiPF_6$ solution in 1:1 (v/v) EC/DMC electrolyte (MilliporeSigma) was dispensed into the cell by pipet. The total electrolyte volume in the cell was ~3 mL.

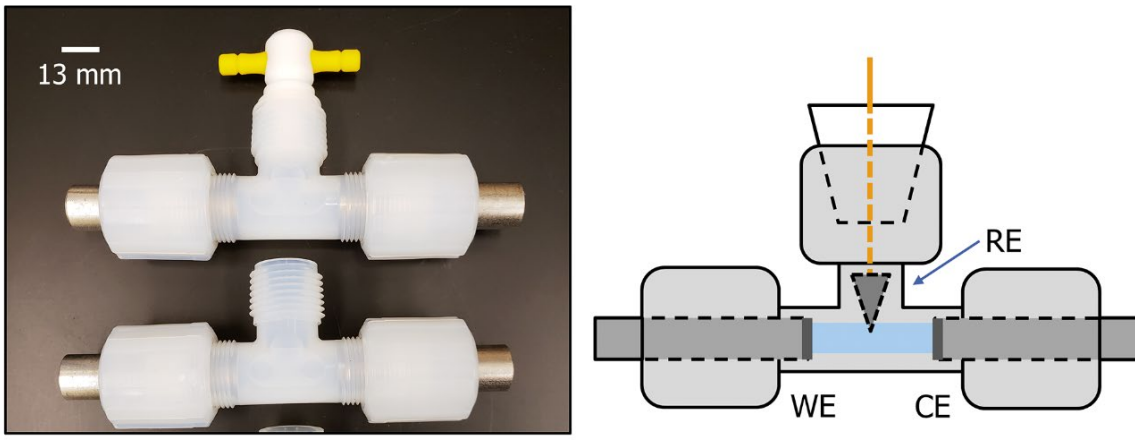

Figure 3.1 - Photograph (*left*) and schematic (*right*) of the tee cell setup used for Li electrodeposition studies.

3.1.2 Methods

Cells were prepared within an Ar-purged glovebox (MBraun). Moisture inside the glovebox was maintained below 5 ppm. A water circulating bath located outside the glovebox pumped chilled or heated water through tubing into a jacketed beaker, controlling the temperature of the electrolyte within the glovebox prior to cell fabrication. After fabrication, the cells were removed from the glove box for electrochemical characterization. During characterization, the temperature of the sealed cells was maintained by immersion in sand at controlled temperatures. The sand was either heated using a hot plate or cooled using refrigeration.

Chronopotentiometry and electrochemical impedance spectroscopy (EIS) experiments were performed using a VersaSTAT 4 potentiostat/galvanostat with built-in frequency response analyzer (Ametek). Chronopotentiometry was performed at an applied current density (i). Here again, i refers to the applied current normalized to the exposed geometric surface area of the WE. For simplicity and consistency, we used the sign

convention that cathodic (plating) current densities and overpotentials are positive quantities. The EIS experiments and analysis were performed using the methods described in Chapter 2. To restate briefly, galvanostatic EIS was performed with a direct current of 0 A and the RMS amplitude was 45 μA cm^{-2}. The frequency range used was 100 kHz to 1 Hz. The ohmic resistance R_e, determined at the high frequency limit, was used to subtract the iR drop in the liquid electrolyte. The surface resistance R_s was determined from the diameter of a circle fit to the Nyquist impedance plot.

The faradaic efficiency of plating was measured via anodic stripping coulometry. A 0.127 mm thick Cu foil (99.9%, Alfa Aesar) was used as substrate for galvanostatic Li plating and subsequent anodic stripping coulometry. Prior to Li plating, the Cu foil was cleaned in 2 M H_2SO_4 for 10 minutes, then rinsed with acetone and deionized water (Millipore). Li plating onto and stripping from the Cu foil were performed in the cell described above. The Cu substrate was used in place of the polished Li foil WE for plating efficiency studies. The electrolyte, RE, and CE were otherwise used in the same manner as above.

3.2 Effects of Temperature on Lithium Electrodeposition

In this section, chronopotentiometry, EIS, and plating efficiency measurements are used to investigate the effects of temperature on Li electrodeposition in order to guide the extension of the Li dendrite initiation model developed in Chapter 2.

3.2.1 Temperature Dependence of Lithium Dendrite Onset Time

The Li dendrite onset time (τ_{onset}) as a function of temperature was investigated under galvanostatic Li electrodeposition. Chronopotentiometry and optical imaging were used to study the initiation and growth of Li dendrites under controlled temperature. After soaking the freshly polished Li WE and CE in liquid electrolyte [1.0 M $LiPF_6$ solution in 1:1 (v/v) EC/DMC] for t_{soak} = 30 min, galvanostatic plating was performed at an applied average current density i = 1 mA cm^{-2} in the tee cell (Fig. 3.1). As demonstrated in Chapter 2, the first appearance of Li dendrites (at $t = \tau_{\text{onset}}$) coincides with the temporal maximum in surface overpotential, $\eta_{\text{s}} = V - iR_{\text{e}}$ (Fig. 3.2). Similar behavior was observed at a variety of temperatures: η_{s} increased during an initial SEI growth phase, reached a local maximum at $t = \tau_{\text{onset}}$, and then decreased during the period of dendrite growth.

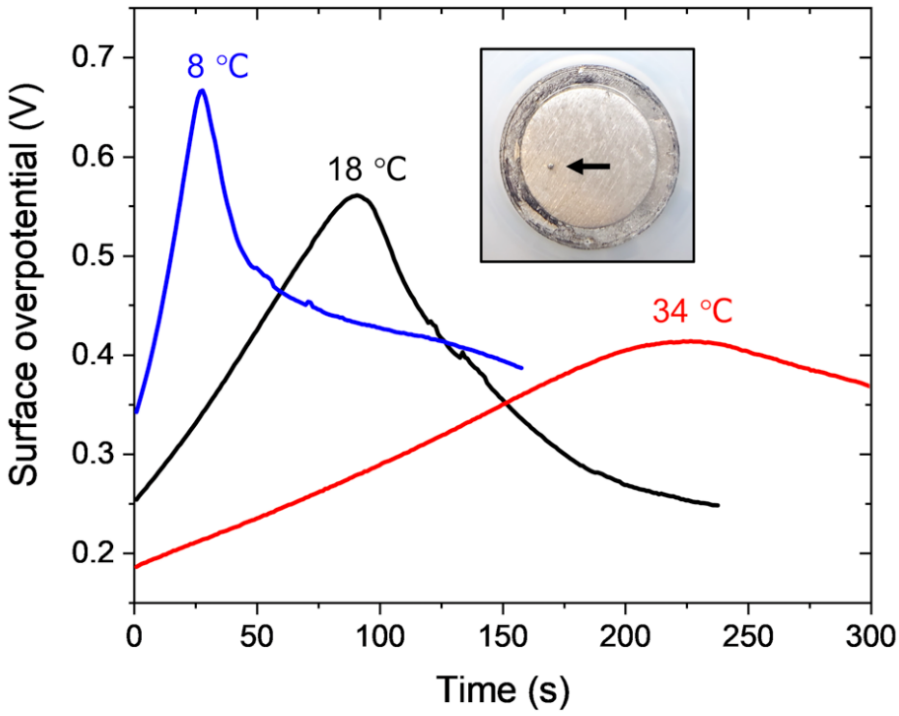

Figure 3.2 - Time-evolution of the surface overpotential during temperature-controlled galvanostatic Li electrodeposition at 1 mA cm^{-2} in 1 M $LiPF_6$ 1:1 EC/DMC. The temperatures were 8 ℃ (*blue*), 18 ℃ (*black*), and 34 ℃ (*red*). The Li electrode was soaked in the electrolyte for $t_{soak} = 30$ min before plating. A photograph (*inset*) of the Li metal surface at $\tau_{onset} = 114$ s, when dendrites first appeared and the surface overpotential η_s reached a local maximum. The plating current density was 1 mA cm^{-2} and the temperature was 24±1.0 ℃ for the experiment shown in the image.

A moderate increase in the temperature of the cell was found to increase τ_{onset}. For instance, at 8 °C the measured τ_{onset} was 30 s, while at 34 °C τ_{onset} was 240 s. Thus, increasing the temperature of Li deposition by 26 °C resulted in an eight-fold increase in the plating time at which the first dendrite appeared. The increase in temperature also lowered the initial $(t = 0)$ surface overpotential, and broadened the peak in the surface overpotential (at $t = \tau_{onset}$). Interestingly, the difference in η_s between $t = \tau_{onset}$ and $t = 0$ was roughly constant (~290 mV) and independent of temperature.

The dependence of τ_{onset} on temperature at i = 1 mA cm^{-2} is shown over the range from 5 to 35 °C (Fig. 3.3). A monotonic increase in dendrite onset time was observed over the range of temperatures studied. This temperature dependence within the range studied does not suggest the presence of a distinct critical temperature below which dendrites are initiated. On the contrary, while Li dendrites were found to initiate at all temperatures, lower temperatures favored an earlier appearance (shorter τ_{onset}) of Li dendrites. This effect of temperature on dendrite initiation will be discussed within the context of Li^+ transport through the SEI layer in the following sections.

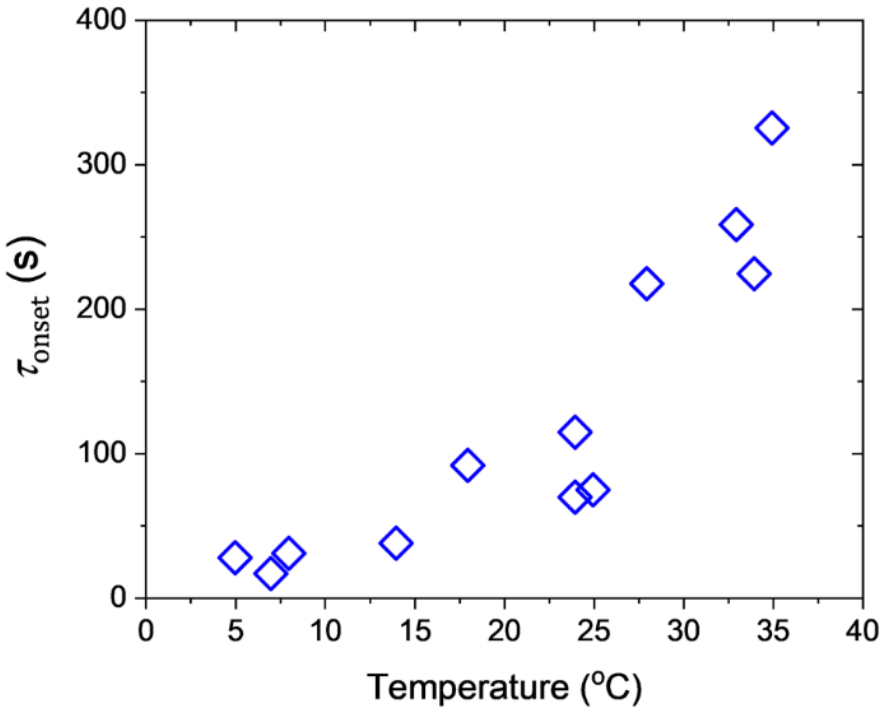

Figure 3.3 - Dendrite onset time (τ_{onset}) as a function of plating temperature. The values of τ_{onset} were determined from the times at which η_s reached a local maximum during chronopotentiometry at current density 1 mA cm^{-2}. The Li foil electrode was soaked in the electrolyte for $t_{\text{soak}} = 30$ min before plating.

3.2.2 Electrochemical Impedance Spectroscopy Measurements

EIS was used to characterize the SEI growth on the Li WE both during the soaking step and during Li electrodeposition. A fixed period ($t_{\mathrm{soak}} = 30$ min) of exposing the Li WE to liquid electrolyte before plating was used to establish an initial SEI before Li electrodeposition. Under open circuit conditions, the surface resistance R_{s} of the WE in contact with liquid electrolyte increased due to SEI growth.[99,100] Nyquist plots for soaking at 22 ℃ are shown in Fig. 3.4a for various values of t_{soak}. In the absence of an externally applied field, as is the case during soaking, the magnitude of R_{s} and thus the SEI thickness[26,82] is expected to increase roughly in proportion to $(t_{\mathrm{soak}})^{\frac{1}{2}}$. This parabolic growth is typical for surface films growing under mass transport limitations of the reacting (*e.g.*, Li^{+}) species.[101] Mathematically, R_{s} depends on t_{soak} as:

$$R_{\mathrm{s}} = (A \cdot t_{\mathrm{soak}})^{\alpha} + B \qquad [3.1]$$

In Eq. [3.1], *A* and *B* are constants. The data in Fig. 3.4b when fitted to Eq. [3.1] provided values of the parameter α, which was 0.5 at 22 °C and 31 °C, but 0.2 at 12 °C. The mechanistic origin of the temperature-dependence of α particularly at low temperatures is presently unknown.

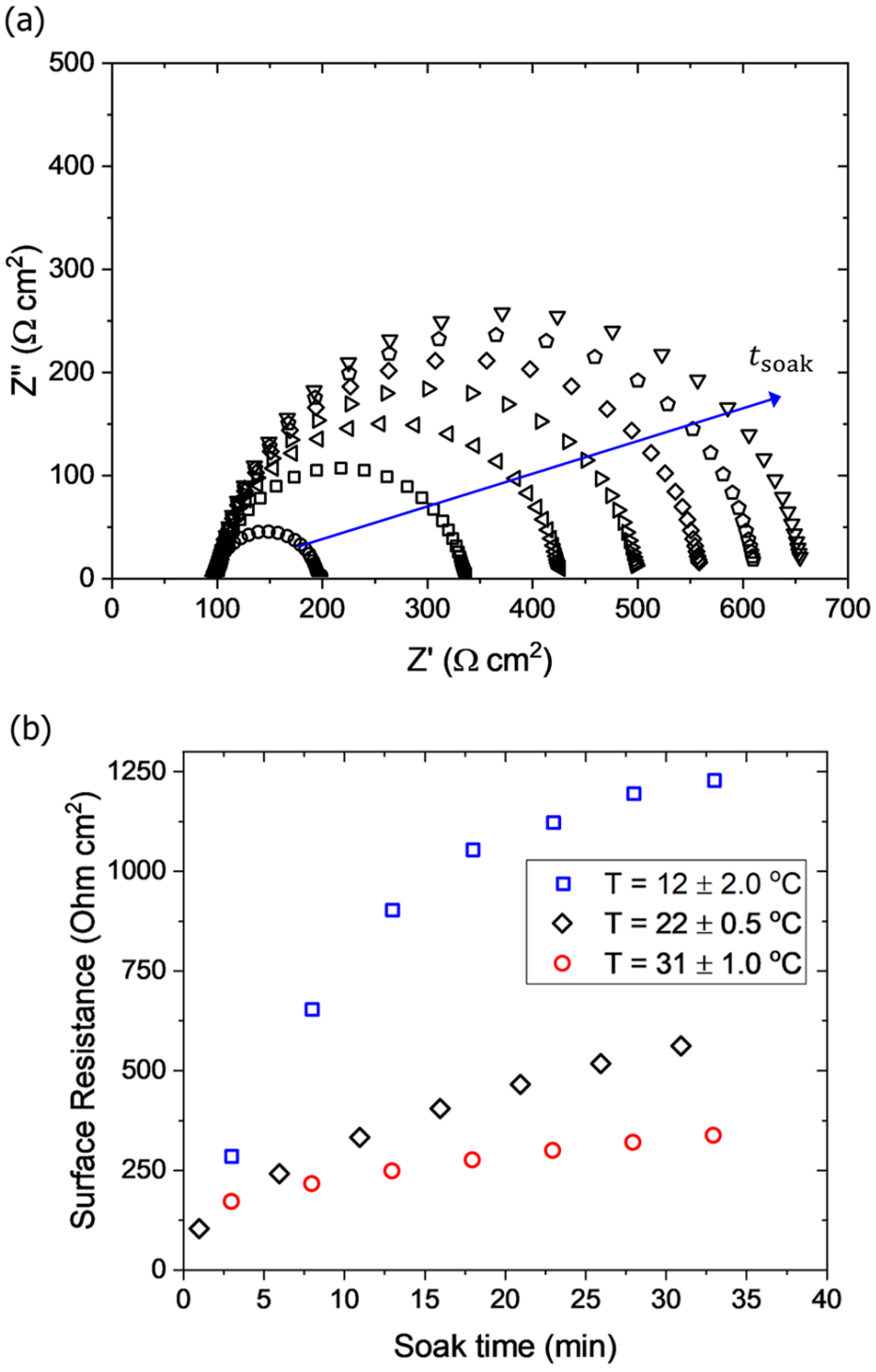

Figure 3.4 - SEI Growth observed by EIS during soak in liquid electrolyte. (a) Nyquist plots at intervals of 300 s during t_{soak} at 22 ℃. The size of the semicircle increased during t_{soak} due to SEI growth. (b) Surface resistance R_s, the diameter of the Nyquist plot semicircle in (a), plotted as a function of t_{soak} at temperatures 12, 22, and 31 ℃.

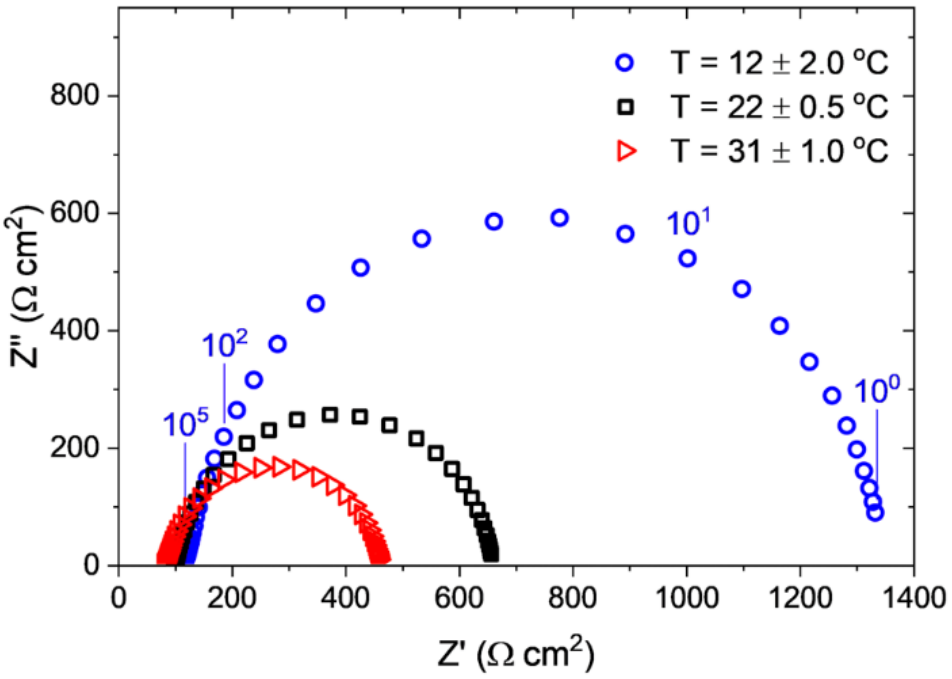

Figure 3.5 - Nyquist plots after $t_{\text{soak}} = 30$ min immediately prior to Li plating at temperatures 12, 22, and 31 °C. The electrolyte resistance R_{e} was weakly temperature-dependent, whereas the Li surface resistance R_{s} was a strong function of temperature.

Nyquist plots immediately prior to plating ($t_{\text{soak}} = 30$ min, $t_{\text{plate}} = 0$ s) are shown for 12, 22, and 31 °C in Fig. 3.5. The electrolyte resistance R_{e} was found to be a weak function of temperature, while the surface resistance R_{s} was observed to be strongly dependent on temperature. The weak temperature-dependence of R_{e}, a liquid-phase property that remains constant during plating, further strengthens the conclusion that liquid-phase transport limitations are not critical in Li dendrite initiation, as was shown in more detail Chapter 2. The solid-state property R_{s} depends on the SEI conductivity κ and the SEI thickness L as:

$$R_s = \frac{L}{\kappa} \qquad [3.2]$$

The quantitative temperature-dependence of κ for the SEI grown in the electrolyte used here and in the temperature range studied is currently unknown. While the theoretical temperature-dependence was given by Peled,[26] we do not have access to the parameters needed to calculate κ. Thus, quantitative determination of L at a variety of temperatures is not feasible for now. We estimate L after t_{soak} to be between 5-10 nm based on $\kappa = 10^{-9}$ S cm^{-1} for Li_2CO_3 at room temperature.[82]

In order to confirm that κ is indeed the relevant temperature-dependent property, EIS measurements were performed on a Li WE immersed in liquid electrolyte while the cell temperature was varied. In this experiment, the Li WE in the cell was allowed to soak for 22 hours until R_s reached an approximately constant value at 35 $\pm$3 ℃. The temperature of the cell was then decreased to 15 ℃ until equilibrium was reached, and EIS was performed again (Fig. 3.6). The figure shows that the value of R_s dropped measurably when the temperature was increased from 15 ℃ to 35 ℃; however, returning the temperature to 15 ℃ produced nearly the same value of R_s as was measured at 15 ℃ before the temperature increase. That is, R_s was roughly the same before (1) and after (3) the temperature increase (2) shown in Fig. 3.6. Such reversibility implies that the SEI thickness L remained relatively constant during the temperature changes, and that R_s changed due to temperature-effects on κ. A rough estimate of the energy barrier for the conduction of Li^+ ions was obtained from the slope of the $ln\ (1/R_s)$ vs. T^{-1} curve. The energy barrier was calculated to be 0.4 eV, which is comparable to the energetics of an ion hopping transport

mechanism reported by Churikov,[61] albeit for a different electrolyte composition. This suggests that transport of Li^+ through the SEI is a temperature-dependent process, and thus it is a factor that must be accounted for in understanding temperature effects on Li dendrite initiation.

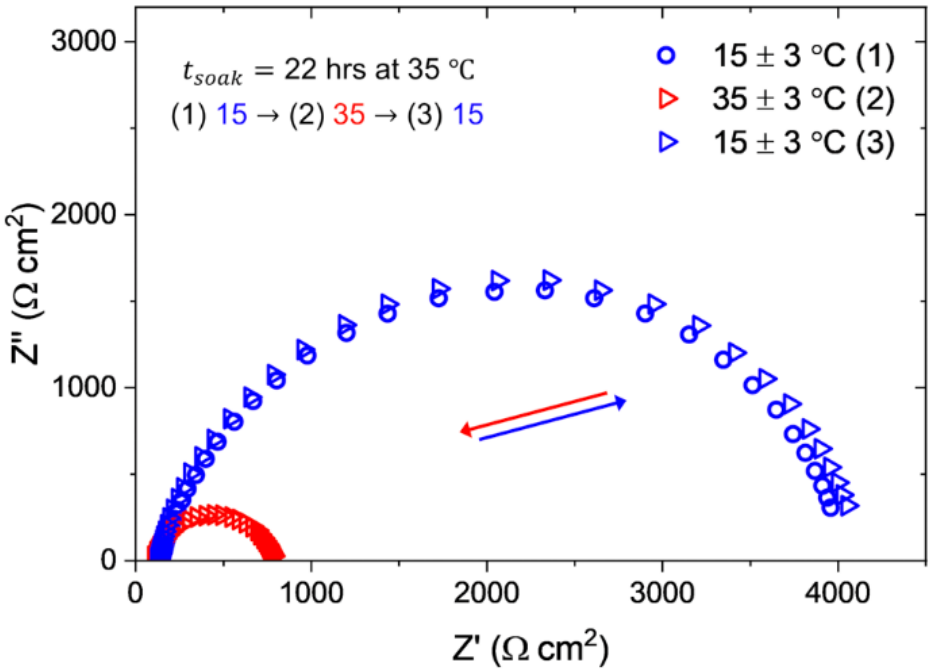

Figure 3.6 - Nyquist plots on a Li electrode over a swing in temperature from 15 ℃ to 35 ℃ and back to 15 ℃. The 3-electrode Li cell was first allowed to soak for 22 hours until R_s reached an approximately constant value at 35±3 ℃ before the cell temperature was lowered. Roughly the same value of R_s was measured at 15 ℃ before (1) and after (3) swinging the temperature to 35 ℃ (2).

For plating experiments in this chapter, the period $t_{soak} = 30$ min when the Li WE was exposed to liquid electrolyte before plating was used to establish an initial SEI after removing the native oxide layer. In Fig. 3.7, the surface resistance R_s is plotted as a function of plating time (t_{plate}) during galvanostatic Li electrodeposition at an applied current

density $i = 1$ mA cm^{-2}. Three temperatures (12, 22, and 31 ℃) were evaluated. During the initial phase of Li plating, *i.e.*, prior to reaching τ_{onset}, a fraction of the applied current is consumed by the formation of additional SEI while the rest of the current results in Li plating. A more quantitative study of these competing processes is conducted in the next section. In Fig. 3.7, the slope of the R_{s} vs. t_{plate} curve must be proportional to the SEI growth rate and inversely proportional to κ in accordance with Eq. [3.2]. This slope is observed to decrease with increasing temperature. Indeed, the general shape of the R_{s} vs. t_{plate} curve (Fig. 3.7) is similar to that of the surface overpotential (η_{s}) time trend seen during galvanostatic Li electrodeposition (Fig. 3.2). This dependence is expected because η_{s} predominantly represents the Li^+ transport resistance through the SEI.[26,60] While the general form of the time evolution of R_{s} and η_{s} are similar, it must be noted that the SEI is not strictly an ohmic resistor.[68] This is evident from comparing the surface resistance R_{s} (= 594 Ω cm^2) at t_{plate} = 15 s and at 22 °C to the surface overpotential η_{s} (= 245 mV) under similar conditions. The surface overpotential (measured at 1 mA cm^{-2}) corresponds to an area normalized surface resistance ($= \eta_{\text{s}}/i$) of 245 Ω cm^2, which is significantly lower than the resistance provided by EIS.

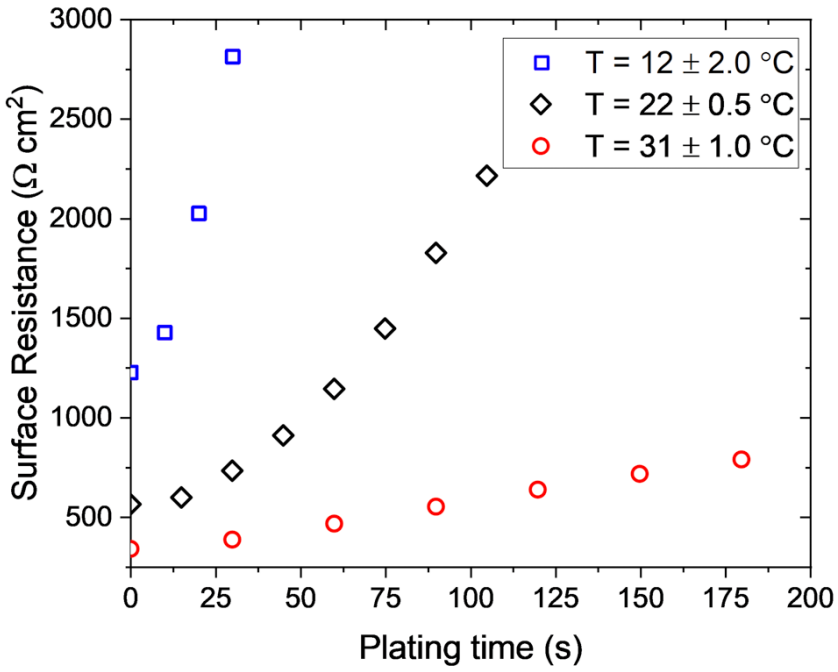

Figure 3.7 - Surface resistance R_s as a function of plating time (t_{plate}) at temperatures 12 °C (*blue*), 22 °C (*black*), and 31 °C (*red*). EIS was performed between periods of galvanostatic Li electrodeposition at $i = 1$ mA cm^{-2} after $t_{soak} = 30$ min.

It should be noted that, while the change in R_s due to temperature was explained by changes in κ, the change in R_s during plating is not due to a temporal change in κ. This was shown by the current interrupt experiments in Chapter 2, where the increase in η_s was irreversible and due to SEI growth as shown by EIS experiments. The rise in R_s and η_s during plating shown in Fig. 3.7 is explained neither by concentration effects nor by conductivity effects. Rather, the increases are due to irreversible SEI growth and continue increasing during plating until dendrites pierce the SEI.

3.2.3 Lithium Plating Efficiency Measurements

Coulometric measurements during Li plating and its subsequent anodic stripping were used to study the effect of temperature on the Li plating efficiency. Li was plated on a Cu substrate in a two-step process. First, an average current density of 2 mA cm^{-2} was applied for 5 seconds to facilitate high nucleation density Li plating on Cu leading to uniform substrate coverage by Li. Next, a current density of 1 mA cm^{-2} was applied for 120 seconds. The Li deposited on the Cu substrate was immediately stripped by applying an anodic potential of +0.5 V vs. Li/Li^+ RE (Fig. 3.8a). The charge corresponding to Li stripping (Q_{strip}) was compared to the total charge passed during plating (Q_{plate}), thus yielding the plating efficiency ε:

$$\varepsilon = \frac{Q_{\text{strip}}}{Q_{\text{plate}}} \qquad [3.3]$$

The difference between Q_{plate} and Q_{strip} accounts for the charge consumed by SEI growth. The experiments were repeated 3 times each at 20±1.0 ℃ and at 30.5±1.0 ℃. As shown in Fig. 3.8b, the Li plating efficiency was not found to be a strong function of temperature. The average ε at 20 ℃ was 44%, while at 30.5 ℃ ε was 48%. The fraction of the charge that contributed to SEI growth during plating was $(1 - \varepsilon)$ and was related to the SEI growth rate as follows:

$$\dot{L} = (1 - \varepsilon)\Gamma i \qquad [3.4]$$

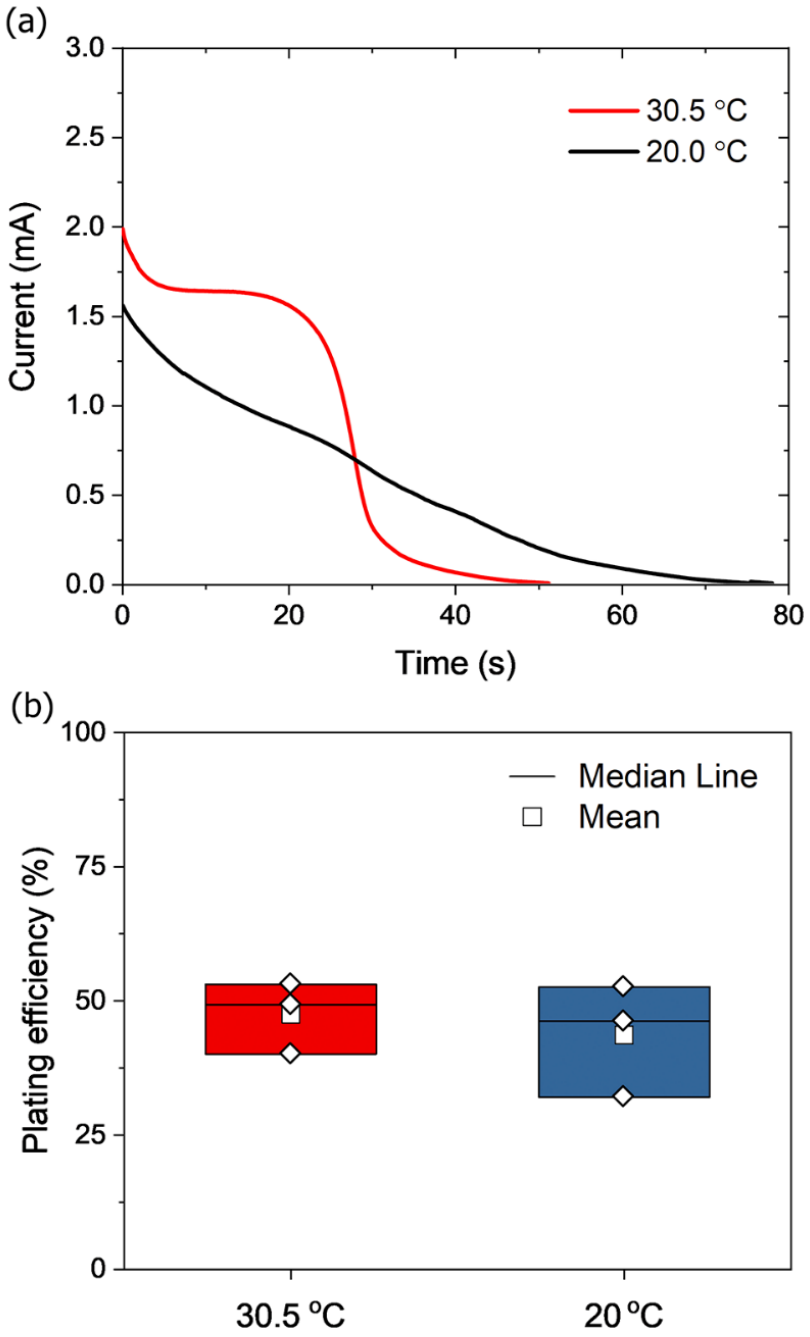

Figure 3.8 - (a) Stripping coulometry at anodic +0.5 V vs. Li/Li^+ on Cu substrates plated with Li performed at 20 °C (*black*) and 30.5 °C (*red*). Prior to stripping, Li was deposited galvanostatically at cathodic 2 mA cm^{-2} for 5 s followed by 1 mA cm^{-2} for 120 s for a total deposition charge $Q_{\text{plate}} = 130$ mC cm^{-2}. (b) Plating efficiency from galvanostatic Li plating and stripping coulometry performed on Cu substrates determined via Eq. 3.3.

In Eq. [3.4], Γ is a constant which incorporates the physicochemical properties of the SEI such as density and molecular weight. Since ε is not a strong function of temperature (Fig. 3.8b), Eq. [3.4] implies that the SEI growth rate $\dot{L}$ at a fixed applied current density i is also relatively independent of temperature. This conclusion will be used in the model development in the following section.

3.3 Transport Model Incorporating Temperature Effects

In this section, the mechanistic model developed in Chapter 2 is extended to explain the increase in Li dendrite onset time with increasing temperature, as reported in Figs. 3.2 and 3.3. Briefly summarizing, the model considers the diffusional transport of Li^+ through a temporally evolving SEI layer. Whereas a typical SEI formed in EC/DMC with $LiPF_6$ salt has a complex bilayer structure with an outer organic layer and an inner compact layer composed of inorganic Li compounds,[33,53] the present model assumes for simplicity a single uniform layer composed of Li_2CO_3. As was demonstrated previously (§2.4.1, §3.2.2), the SEI layer grows in thickness on the Li surface during soaking as well as during Li electrodeposition. Transport of Li^+ through this evolving SEI is shown schematically in Fig. 3.9. The SEI growth that occurs during the time period t_{soak} (prior to the start of Li plating) forms the initial SEI thickness L_0. During Li electrodeposition, the SEI grows at a roughly constant rate $\dot{L}$ proportional to $(1 - \varepsilon)$ as in Eq. [3.4]. The steady growth of the SEI layer manifests in experiments as a steady increase in the surface resistance R_{s} seen in EIS data, and a steady increase in the surface overpotential η_{s} seen in chronopotentiometry.

To model transport of Li^+ ions across the SEI, we neglect electric field induced migrational transport. The SEI can be thought of as an electrolyte in which the Li^+ transference number is very small ($t_+ \ll 1$; *i.e.*, migrational transport is negligible). We also assume that a linear Li^+ concentration profile develops within the SEI, and that this drives diffusion as the dominant mode of Li^+ transport. Simulations in Chapter 4 support the assumption of a linear concentration profile in this model. Chapter 2 showed the importance of solid-state diffusion through the SEI, since the applied current density approaches the limiting current in the solid state.

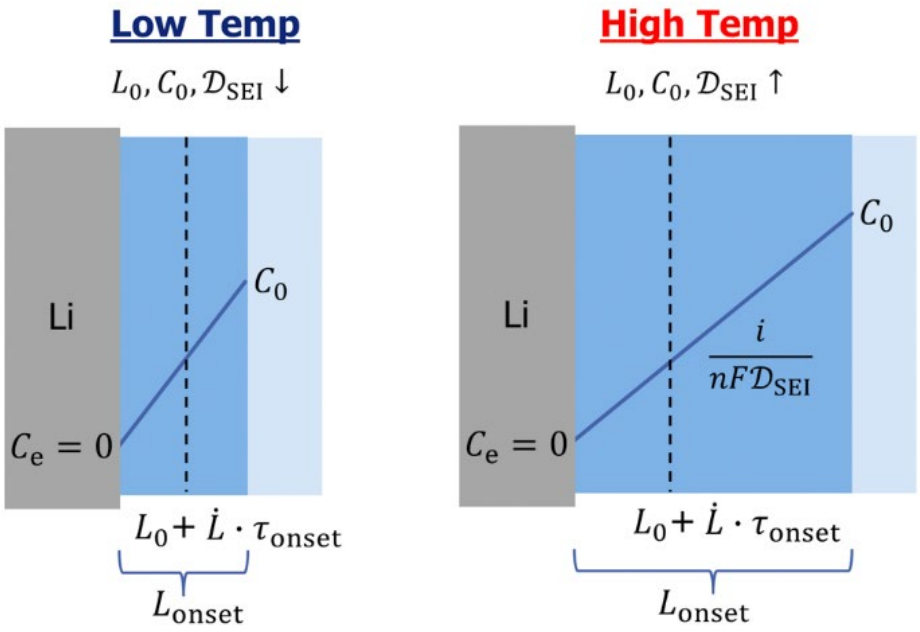

Figure 3.9 - Schematic showing Li electrodes submerged in liquid electrolyte and covered with SEI of thickness L_{onset}. During t_{soak}, the SEI grows to thickness L_0. During t_{plate}, the SEI continues to grow at the rate $\dot{L}$. The concentration gradient with slope $i/nF\mathcal{D}_{SEI}$ develops due to the consumption of Li^+ at the Li-SEI interface. At low temperatures, the bulk concentration of Li^+ (C_0) is lower and the concentration gradient is steeper due to lower $\mathcal{D}_{SEI}$. Faster dendrite initiation time τ_{onset} at low temperatures is explained by the increased resistance associated with Li^+ diffusional transport.

At pseudo-steady state, the Li^+ diffusional flux is proportional to the applied current density i. Under galvanostatic conditions, this provides the Li^+ concentration at the Li-SEI interface (C_e):

$$C_e = C_0 - \frac{iL}{nF\mathcal{D}_{SEI}} \quad [3.5]$$

As before, C_0 is a constant Li^+ concentration in the SEI at the SEI-electrolyte interface (Fig. 3.9), and $\mathcal{D}_{SEI}$ is the solid-state Li^+ diffusion coefficient in the SEI. During Li plating, the SEI layer thickness L increases due to competing reduction of the electrolyte. The increase in thickness causes the gradual depletion of Li^+ at the Li-SEI interface. Eventually, as the plating time reaches τ_{onset}, C_e approaches 0 and, as demonstrated in Chapter 2, this depletion is responsible for the initiation of Li dendrites. Assuming that L increases linearly with time ($L = L_0 + \dot{L}t_{plate}$), the critical time τ_{onset} at which C_e approaches 0 leading to onset of dendrites is:

$$\tau_{onset} = \frac{1}{\dot{L}}\left(\frac{nF\mathcal{D}_{SEI}C_0}{i} - L_0\right) \quad [3.6]$$

Eq. [3.6] provides insights into the effect of temperature on τ_{onset}. First, as described above (Eq. [3.4] and related discussion), the SEI growth rate $\dot{L}$ at a fixed applied current density i is not a strong function of temperature. Furthermore, the initial thickness L_0 (which depends on t_{soak}) should increase with temperature because of faster transport through the SEI at elevated temperatures; however, per Eq. [3.6], this effect would lead to a decrease

in τ_{onset} at higher temperatures, which is inconsistent with the experimental data in Figs. 3.2 and 3.3. Thus, temperature-dependencies of $\dot{L}$ and L_0 do not explain the temperature-dependence of τ_{onset}. Instead, the lumped parameters $\mathcal{D}_{\text{SEI}}C_0$ comprising the diffusion coefficient ($\mathcal{D}_{\text{SEI}}$) and the maximum concentration of mobile Li^+ species in the SEI (C_0) are relevant to temperature effects. Although the precise temperature-dependence of $\mathcal{D}_{\text{SEI}}C_0$ is not known, both parameters $\mathcal{D}_{\text{SEI}}$ and C_0 are expected to increase with temperature, causing an increase in τ_{onset} per Eq. [3.6]. Therefore, one or both of these parameters is responsible for the strong influence of temperature on τ_{onset}. At low temperatures, fewer defects are present in the SEI (lower value of C_0) and solid-state diffusivity ($\mathcal{D}_{\text{SEI}}$) is also lowered.[53,69,70] These factors are responsible for lower an earlier onset of Li dendrite growth. At higher temperatures, a greater number of defects (C_0) and an elevated diffusion coefficient ($\mathcal{D}_{\text{SEI}}$) permits the SEI to grow to a greater thickness L before reaching the critical condition $C_{\text{e}} \rightarrow 0$ for dendrite initiation. Consequently, at elevated temperatures, Li dendrite initiation is delayed. Thus, our model qualitatively explains the observed temperature-dependence of τ_{onset} based on changes in Li^+ transport ($\mathcal{D}_{\text{SEI}}C_0$) through the SEI.

3.4 Conclusions

The temperature-dependence of Li dendrite initiation during galvanostatic electrodeposition was investigated using experiments and modeling. The following main conclusions are drawn from this chapter:

(i) Li dendrite initiation time ($t = \tau_{\text{onset}}$) during galvanostatic Li electrodeposition was found to increase monotonically with an increase in temperature from 5 ℃ to 35℃.

(ii) During Li electrodeposition at all temperatures studied, the SEI continued to grow in thickness (for $t < \tau_{\text{onset}}$), as evidenced by an increase in surface overpotential and surface resistance, until the onset of dendritic growth.

(iii) Increasing temperature increases the solid state ionic conductivity (κ) of the SEI.

(iv) The Li plating efficiency, and thus the SEI growth rate during galvanostatic electrodeposition, was shown not to be a strong function of temperature.

(v) The temperature-dependence of the Li dendrite initiation time was explained within the framework of the Li^+ transport model developed in Chapter 2. The bulk concentration C_0 and diffusion coefficient $\mathcal{D}_{\text{SEI}}$ of Li^+ within the SEI are suggested to be the temperature-dependent parameters responsible for the increase in τ_{onset} with increasing temperature, per Eq. [3.6].

The sluggish transport of Li^+ through the SEI imposes a major limitation during low-temperature charging of Li-metal batteries. The slower transport leads to faster depletion of Li^+ at the Li-SEI interface, triggering earlier initiation of Li dendrites at lower temperatures. Our work implies that while Li dendrite initiation during battery charging may be inevitable, even at low current densities, avoiding low temperatures, and thereby facilitating faster Li^+ transport, is critically essential in delaying dendrites.

CHAPTER 4. Pulsed Current Lithium Plating: Continuum Simulations of Li^+ Diffusion in the SEI

Several strategies have been reviewed in the literature for their potential to mitigate Li dendrites. These strategies include organic additives to form a more stable SEI,[102-104] artificial SEI layers,[105-107] ionic liquid electrolytes,[108,109] and pulsed current charging.[92,93] Some of these methods have also been applied to improve the charging of Li-ion batteries.[110-112] In §2.5, pulsed current electrodeposition was used to mitigate the concentration depletion experienced at the Li metal-SEI interface. The results of pulsed current Li plating provided support for the model proposed in §2.4. However, it remains to be shown whether pulsed current Li plating does in fact provide practical advantages for charging Li-metal batteries, since it is desirable to maintain high average charging rates. Although the Li surface shown in Fig. 2.11 appears smooth after p.c. compared to d.c. plating, the charging rate was severely reduced. The question is whether p.c. provides an advantage over d.c. charging when the comparison is made at matched charging rates, particularly given the complexities of SEI growth and the Li^+ transport through the solid film.

In this chapter, numerical simulations are performed with the aim to understand the effects of pulsing on the Li^+ concentration gradients that develop within the SEI. A time-dependent diffusion-reaction model for a growing SEI domain is developed and solved numerically using COMSOL®. This analysis leads to the conclusion that pulsed current provides no intrinsic advantage over d.c. during the charging of Li-metal batteries.

4.1 Mathematical Model

In this section, the model of Li^+ transport and reaction within the SEI is developed. As in Chapters 2 and 3, the Li^+ transport through an SEI of thickness L is modeled in 1D (Fig. 4.1). The Li plating reaction is assumed to take place at the Li metal-SEI interface ($x = 0$). A competing cathodic reaction, described as SEI growth (§2.4.1), occurs in conjunction with Li plating.[20] The model assumes this side reaction to be the reduction of ethylene carbonate (EC), which forms the solid Li_2CO_3 layer that makes up the SEI.[54] In reality, the SEI may be composed of a compact layer of numerous inorganic Li species covered by a porous outer layer of organic compounds, as described in (§3.3). However, we use a single layer to model the transport processes within the SEI.

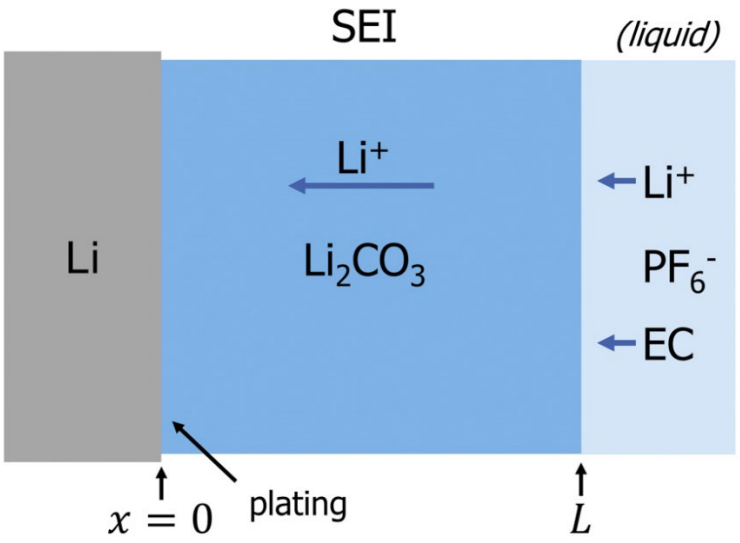

Figure 4.1 - Schematic of the 1D model: a Li electrode in liquid electrolyte is covered with an SEI of thickness L. Li plating occurs at the interface between the Li metal electrode and the SEI ($x = 0$). The Li electrodeposition reaction competes with the cathodic SEI formation reaction, resulting in a gradual increase in L over time.

4.1.1 Transport Equation

In Chapter 2, a model for the Li dendrite initiation time (τ_{onset}) was developed wherein Li^+ diffusion was assumed to be the dominant transport mechanism within the growing SEI. The governing equation for transient diffusion processes is Fick's second law. In one dimension, Eq. 4.1 describes Fickian diffusion of Li^+ within the SEI,

$$\frac{\partial C^*}{\partial t} = \mathcal{D}_{\text{SEI}} \frac{\partial^2 C^*}{\partial x^2} \qquad [4.1]$$

where C^* is the dimensionless concentration of Li^+ defects, C/C_0. The value of C_0 was assumed to be 10^{-5} mol cm^{-3} and $\mathcal{D}_{\text{SEI}}$ was taken as 10^{-9} cm^2 s^{-1} as in Chapter 2.

It should be emphasized that knowledge of the parameters ($\mathcal{D}_{\text{SEI}}, C_0$) involved in Li^+ transport through SEI is currently limited. In fact, the precision is within an order of magnitude at best due to the range of species present in the SEI and the difficulties in characterizing them precisely on a Li surface.[113] This lack of precision should not dissuade one from the mechanistic insight that can still be gained through such modeling analysis.

4.1.2 Initial and Boundary Conditions

The differential equation [4.1] requires one initial condition and two boundary conditions. A uniform concentration profile $C^* = 1$ is assumed for the initial condition ($t = 0$). The boundary condition at $x = L$ is a fixed concentration, also $C^* = 1$. The boundary condition at $x = 0$ is a constant flux due to galvanostatic conditions (current density i):

$$\mathcal{D}_{\mathrm{SEI}}\nabla C^{*} = \frac{i}{nFC_0} \qquad [4.2]$$

where ∇C^{*} is the gradient of the normalized concentration of Li^{+} at the Li-SEI interface. The values of the parameters used in Eq. 4.2 are shown in Table 4.1.

Table 4.1 – Parameters for the diffusion-reaction model used to simulate d.c. and p.c. Li plating.[a]

Parameter	Direct Current	Pulsed Current
Current density, i_{on}	0.5 mA cm^{-2}	1 mA cm^{-2}
SEI growth rate, $\dot{L}$	2.0×10^{-2} nm s^{-1}	4.5×10^{-2} nm s^{-1}
Intial SEI thickness, L_0	8 nm	8 nm
Plating efficiency, ε	0.7	0.4
Duty cycle, σ	1	0.5
Pulse length, t_{on}	-	0.1, 1, 10, 1000 ms

For pulsed current (p.c.) simulations, a square wave controls the flux at the boundary $x = 0$ (Fig 4.2). During t_{off}, $i_{\mathrm{off}} = 0$. The duty cycle σ quantifies the fraction of the period when the current is on, given by Eq. 4.3:

[a] The SEI growth rates $\dot{L}$ were determined by EIS in the manner shown in §2.3. Plating efficiencies ε were determined by stripping coulometry on a Cu substrate, as shown in Chapters 2 and 3.

$$\sigma = \frac{t_{\text{on}}}{t_{on} + t_{\text{off}}} \qquad [4.3]$$

The parameter σ can be chosen from 0 to 1, where $\sigma = 1$ is the d.c condition. Adjusting this parameter provides additional control that is not available in d.c. plating. For example, the concentration depletion (during t_{on}) can be replenished via diffusion (during t_{off}), and these two times can be adjusted independently. However, a single value of $\sigma = 0.5$ was used in this work to simplify the analysis. To maintain the same average plating (charging) rate by compensating for the time when the current is off during p.c., the product $i_{\text{on}} \cdot \sigma$ was matched for d.c. and p.c. plating (Fig. 4.2). For $\sigma = 0.5$, this implies that $[i_{\text{on}}]_{\text{p.c.}} = 2[i]_{\text{d.c.}}$ as is shown in Table 4.1.

In reality, the SEI grows at the rate $\dot{L}$ only during t_{on}, the fraction of the pulse when the current is on. Rather than modeling SEI growth as stepwise during pulsing, for simplicity, $\dot{L}$ is multiplied by the duty cycle σ so that the domain grows at a constant linear rate:

$$L = L_0 + \dot{L}t\sigma \qquad [4.4]$$

where t is the plating time that includes both t_{on} and t_{off}. This means that the SEI growth occurs at a constant average rate during p.c. plating, rather than only during t_{on}. This modification is justified when the change in SEI thickness during any given pulse cycle is small in comparison to the overall change during the entire pulse train.

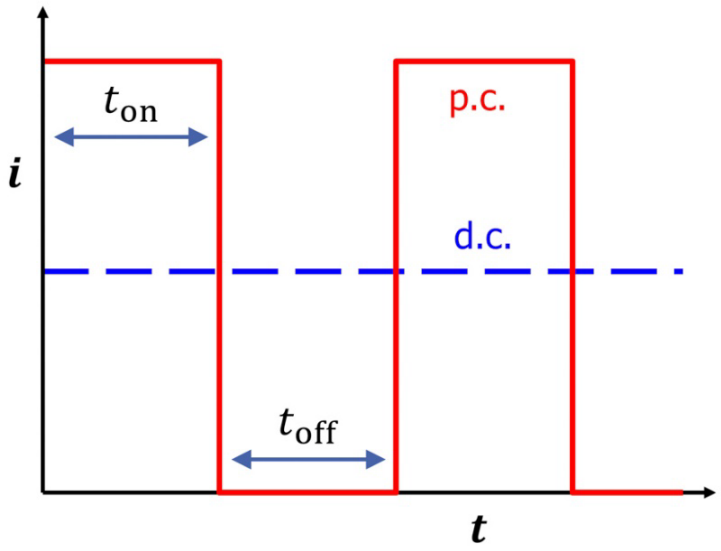

Figure 4.2 - Schematic of applied current density (i) vs. time (t) for d.c. and p.c. Li plating simulations. For a duty cycle $\sigma = 0.5$, the i_{on} of p.c. plating must be double that of d.c. plating to achieve equivalent plating rates. Thus, given d.c. $i_{on} = 0.5$ mA cm^{-2}, p.c. $i_{on} = 1.0$ mA cm^{-2}.

4.2 Simulation Results and Discussion

In this section, numerical solutions to Eq. 4.1 (with initial and boundary conditions described in §4.1.2) were obtained using COMSOL Multiphysics® version 5.4. The solutions provided concentration profiles of Li^+ within the SEI on a Li electrode during direct current (d.c.) and pulsed current (p.c.) plating. A comparison between d.c. and p.c. plated charge was used to analyze whether p.c. Li plating provides any practical advantages during the recharge of Li-metal batteries.

4.2.1 Direct Current (d.c.) Simulations

Figure 4.3 illustrates the Li^+ concentration profile that develops within a growing SEI when constant cathodic current (0.5 mA cm^{-2}) is applied. During electrodepostion, Li^+ is consumed and deposited as Li^0 at the Li metal-SEI interface ($x = 0$). At short times (0.1 ms or less), the normalized interfacial concentration C_e^* at $x = 0$ decreases with plating time as the concentration profile develops. After ~1 ms, a linear Li^+ concentration profile is present within the SEI (Fig. 4.3). After 1 s of d.c. plating, the Li^+ concentration gradient remains constant, but C_e^* gradually decreases as the SEI thickness L increases over ~1000 s of Li plating.

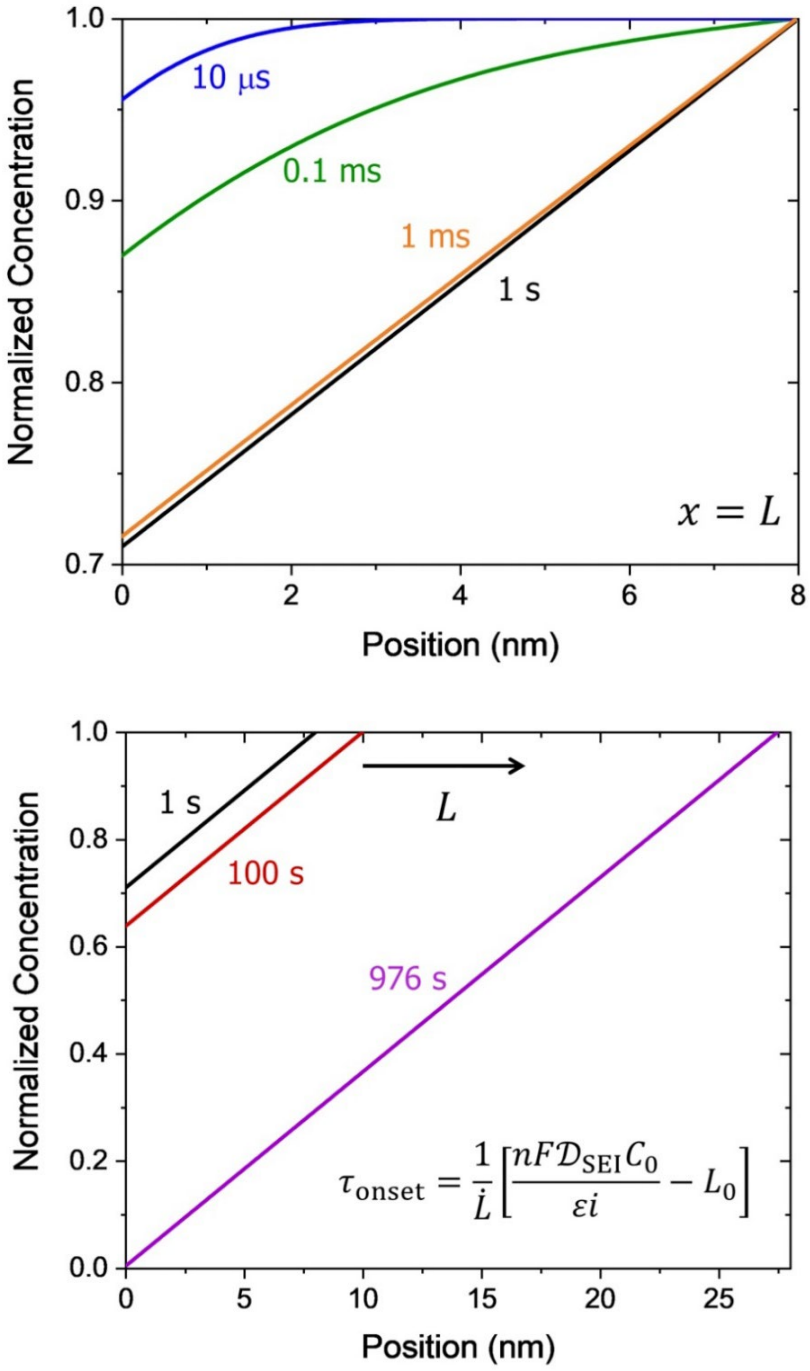

Figure 4.3 - Normalized Li^+ concentration C^* as a function of position within the growing thickness L of the SEI during d.c. Li plating at 0.5 mA cm^{-2}. The Li^+ concentration profiles shown are after 10 μs (*blue*), 0.1 ms (*green*), 1 ms (*orange*), 1 s (black), 100 s (*deep red*), 976 s (*purple*). A linear concentration gradient develops after ~ 1 ms. As plating progresses, the concentration C_e^* of Li^+ at $x = 0$ decreases at a linear rate due to SEI growth. After 100 s, L increased by ~2 nm. At 976 s ($t = \tau_{\text{onset}}$), L is about 27 nm and $C_e^* = 0$ (condition for dendrite initiation).

Beyond 1 s, the slope of the Li^+ concentration gradient remains constant while the thickness of the SEI L continues to increase at a constant SEI growth rate $\dot{L}$ (Fig. 4.3). Because of this growth, the normalized concentration of Li^+ at $x = 0$ (C_e^*) slowly but steadily decreases during d.c. plating. It is noteworthy that the time constant for pseudo-steady state to develop (~1 ms) is much less than the time required for significant SEI growth ($\gg$ 1 s). For example, the SEI grows only 2 nm in 100 s of d.c. plating at 0.5 mA cm^{-2}. Thus, the assumption of a linear concentration gradient is valid in our analytical model (§2.4) for the time τ_{onset} when dendrites initiate during galvanostatic d.c. plating. The analytical model is represented by:

$$\tau_{\text{onset}} = \frac{1}{\dot{L}}\left[\frac{nF\mathcal{D}_{\text{SEI}}C_0}{\varepsilon i} - L_0\right] \qquad [4.5]$$

where the parameters are given in Table 4.1. Here, we account for the plating efficiency, which was shown to differ between d.c. and p.c. plating (§2.5).

The time at which C_e^* reaches 0 is defined as τ_{onset} because this condition is responsible for dendritic Li electrodeposition (§2.4.2). For the same input parameters, Eq. 4.2 yields the same τ_{onset} as the numerical solution of equation 4.1, *i.e.*, 976 s (Fig. 4.3). The close agreement between numerical and analytical results gives us confidence that the 1D model adequately represents the key transport processes that are responsible for Li dendrite initiation: diffusion limitations of Li^+ within the SEI caused by continuous SEI growth. The analytical model also agrees with experimental results for a variety of conditions, including initial SEI thickness, current density, and temperature, as shown in Chapters 2 and 3. Having shown that the 1D numerical model agrees with the analytical

solution for d.c. plating, we now make use of these results for comparing Li^+ concentration profiles between d.c. and p.c. plating.

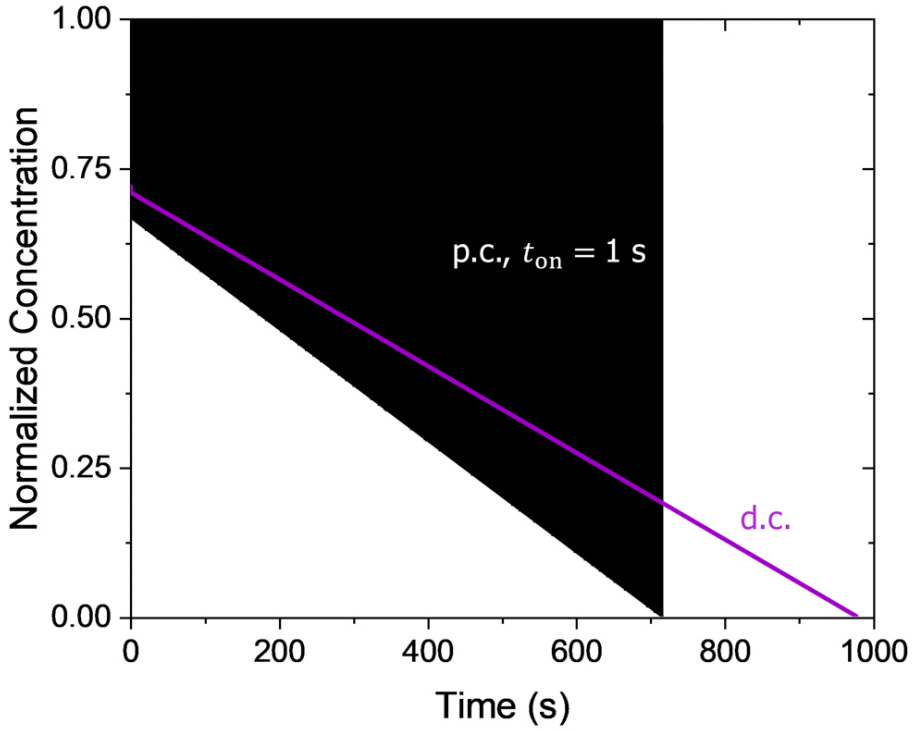

Figure 4.4 - Normalized Li^+ concentration C_e^* at the $x = 0$ Li electrode-SEI interface vs. plating time for d.c. (*purple*) and p.c. (*black*). The d.c. current density was 0.5 mA cm^{-2}, while the p.c. current density was 1 mA cm^{-2} and the duty cycle (σ) was 0.5. For d.c. and p.c. plating, τ_{onset} times were 978 and 718 s, respectively. The pulse length used for the p.c. condition was $t_{on} = 1$ s. The densely packed black line oscillates when current is turned on and off, as shown in greater detail in Fig. 4.5.

4.2.2 Pulsed Current Simulations

Figure 4.4 shows C_e^* as a function of time during d.c. and p.c. plating. Again, C_e^* drops from ~0.7 at 1 s to 0 after 976 s of d.c. plating at 0.5 mA cm^{-2} due to continuous SEI growth. On the other hand, C_e^* oscillates during p.c. plating (Fig. 4.4) depending on whether current is on or off. With a duty cycle σ of 0.5, it is necessary to double the current density

i_{on} during p.c. in order to match the average plating rate at 0.5 mA cm^{-2} for d.c. (Fig. 4.2). Plating at $i_{\mathrm{on}} = 1$ mA cm^{-2} with $t_{\mathrm{on}} = 1$ s and $\sigma = 0.5$, the concentration C_{e}^{*} reaches 0 at a faster rate compared to d.c., even though the concentration gradient fully relaxes during each pulsing cycle (Fig. 4.4). The shorter τ_{onset} during p.c. is due to two factors: (i) the faster SEI growth rate $\dot{L}$ at a higher current density, and (ii) the pulse is long enough for a linear concentration gradient to develop, as in d.c. plating. Similarly, for p.c. plating at 1 mA cm^{-2} with $t_{\mathrm{on}} = 10$ ms and $\sigma = 0.5$, the rate at which the minimum C_{e}^{*} (for a given pulse) decreases is equal to that when $t_{\mathrm{on}} = 1$ s (Fig. 4.5 *top*). The effect of pulsing when $t_{\mathrm{on}} = 10$ ms or 1 s is the same: pseudo-steady state is established before the end of the pulse. It is pseudo-steady because, although the concentration gradient fully develops during the time of a single pulse, the SEI continues to grow during the plating process. While SEI growth is not significant during a single pulse, it does affect the concentration profile over a longer time scale, as will be shown later.

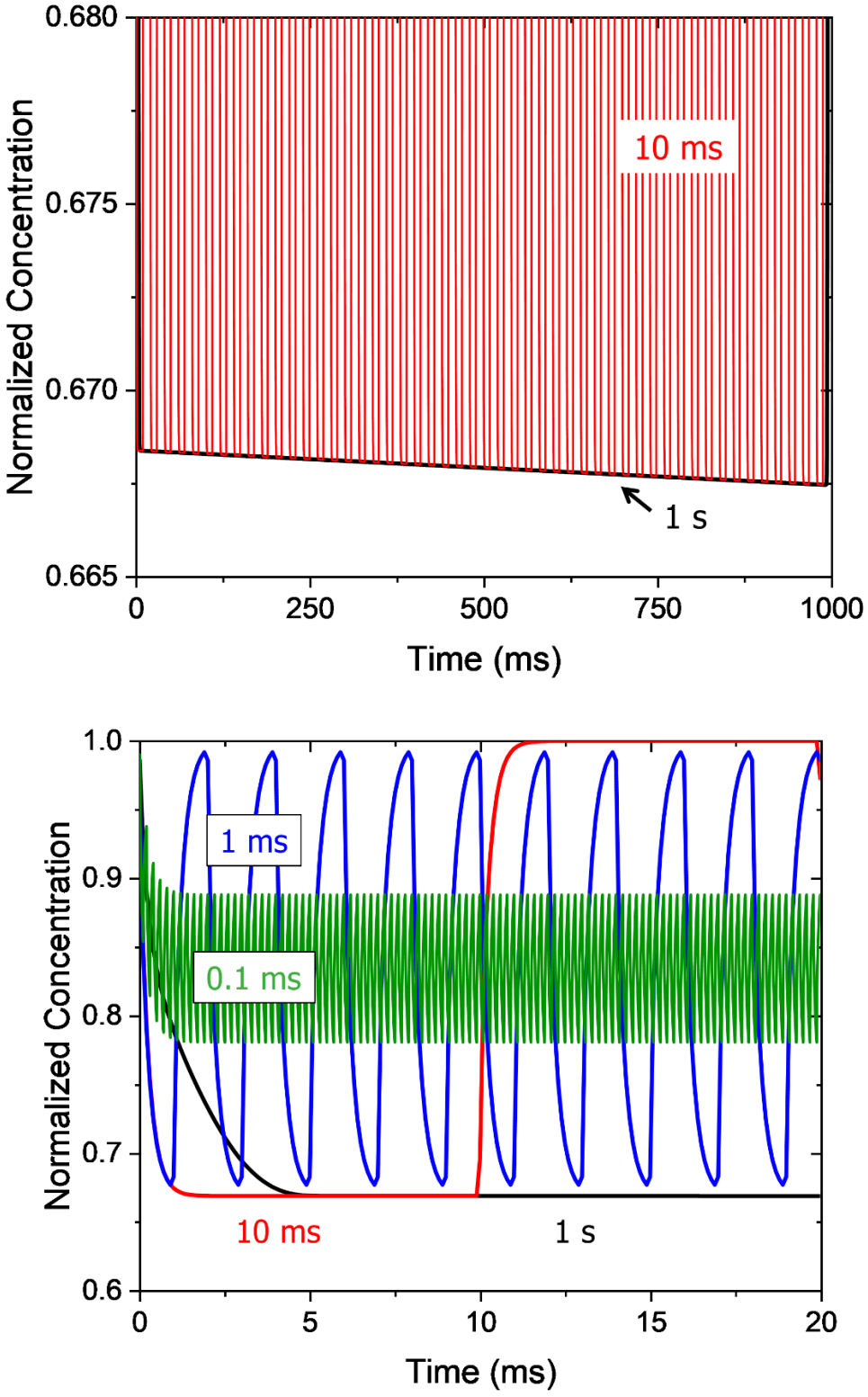

Figure 4.5 - Normalized Li^+ concentration C_e^* at $x = 0$ (Li electrode-SEI interface) vs. time during p.c. plating. The pulse 'on' times t_{on} were 1 s (*black*), 10 ms (*red*), 1 ms (*blue*), and 0.1 ms (*green*).

The simulation results illustrate that full relaxation of the concentration gradient (while the current is off) is not essential, nor is it always beneficial in preventing dendritic plating. Instead, p.c. can delay τ_{onset} when linear concentration gradient during pulsing is prevented. The pulsating zone, the region of space in which concentration fluctuates over a single pulse, narrows when the pulse length t_{on} is reduced.[114] When t_{on} is 1 ms or less, the concentration profile remains transient throughout the pulsing train. In this case, pseudo-steady state is not reached, and C_{e}^{*} oscillates in a narrower band (Fig. 4.5 *bottom*). When t_{on} is 0.1 ms, the range of C_{e}^{*} is even narrower, as indicated by the green band of values in Fig. 4.5. The longer C_{e}^{*} remains above 0, the longer it takes for dendrites to be initiated. Shortening t_{on} maintains a greater C_{e}^{*} during plating; however, when t_{on} is equal to or less than the time needed for double layer charging (~1 μs), no faradaic reaction takes place and thus, no Li is plated. In light of this consideration, 0.1 ms was chosen as the minimum pulse length for the simulations.

Although pulsing at a very fast rate (*i.e.*, $t_{\text{on}} < C_0 LnF/2i$, the time constant for pseudo-steady state to develop) may delay dendrites (increase τ_{onset}) by maintaining a higher C_{e}^{*} for a longer plating time, the delay does not imply that p.c. offers any intrinsic advantages over d.c. that can be exploited by Li-metal battery charging systems. A more thorough comparison between d.c. and p.c. Li plating is discussed in the next section.

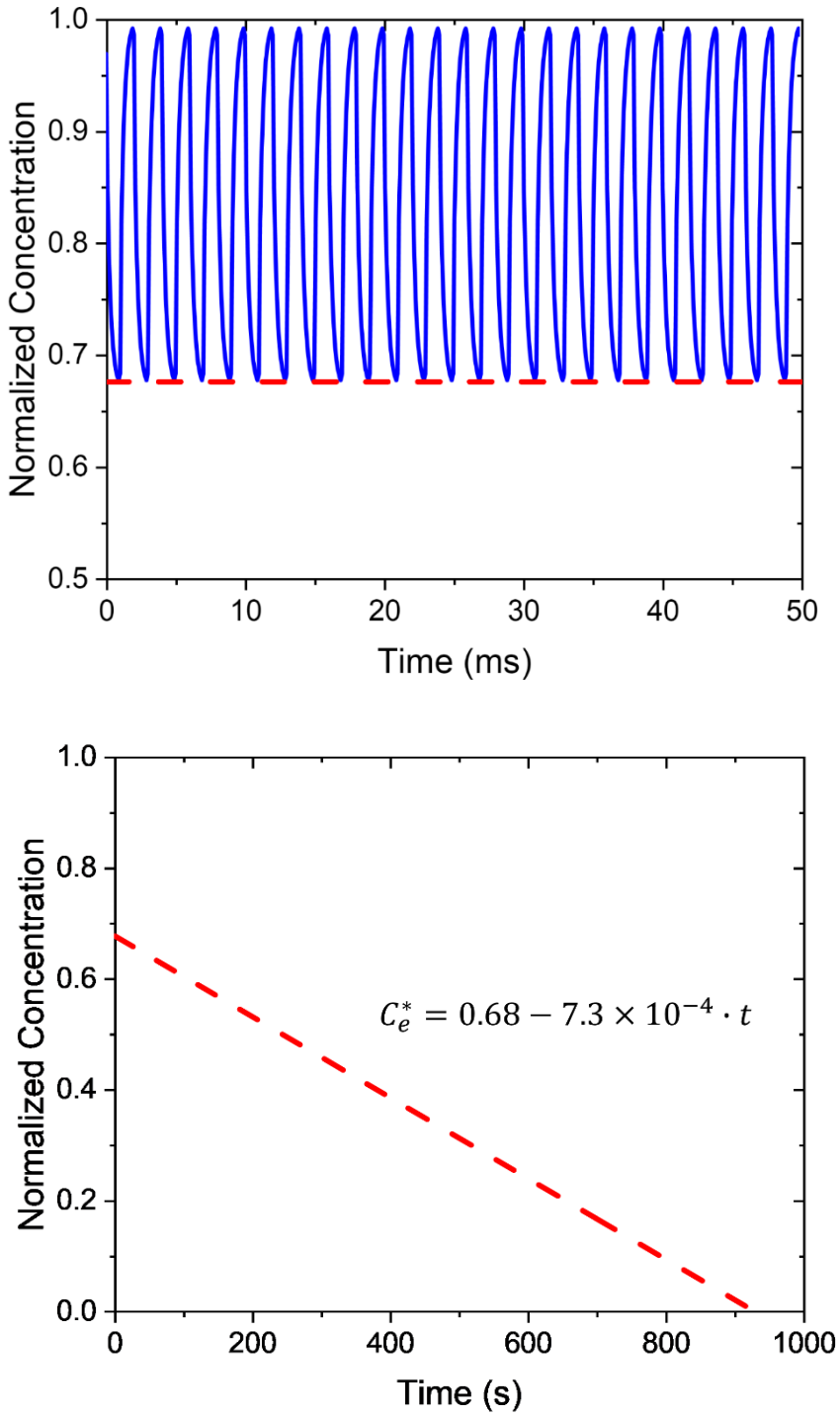

Figure 4.6 - Extrapolation method for determining τ_{onset} from a fit to the minimum C_{e}^* values at the end of t_{on} as a function of the p.c. plating time. The normalized Li^+ concentration C_{e}^* for $t_{\text{on}} = 1$ ms (*blue*) at short times is used for a linear fit that is extrapolated to long times (*red dashed*). The equation of the linear fit is shown (*bottom*).

4.2.3 Quantitative Comparison of Li Plated by p.c. and d.c. before Dendrite Onset

In order to make a comparison between d.c. and p.c. for equivalent Li plating rates, the total charge density Q of plated Li metal prior to the onset of dendrites is estimated by Eq. 4.3:

$$Q = i\sigma\varepsilon\tau_{\text{onset}} \quad [4.3]$$

Eq. 4.3 incorporates the duty cycle σ as well as the plating efficiency ε. The values of the parameters used in computing Q via Eq. 4.3 are shown in Table 4.1. Values for τ_{onset} were determined via simulations for d.c. (Fig. 4.3) as well as p.c. with $t_{\text{on}} = 1$ s and 10 ms. For $t_{\text{on}} = 1$ ms and 0.1 ms, τ_{onset} values were determined using extrapolations from a linear fit to the minimum values of the $x = 0$ surface concentration C_{e}^{*}, as illustrated in Fig. 4.6. Since the concentration C_{e}^{*} at the end of t_{on}decreases over time due to linear SEI growth, linear extrapolation to τ_{onset} (when C_{e}^{*} reaches 0) is justified. Values for τ_{onset} and the resulting plated charge densities Q are shown in Fig. 4.7. The Q achieved by p.c. is less than d.c for all conditions evaluated, including the shortest t_{on}, 0.1 ms. This suggests that, for equivalent charging rates in Li-metal batteries, p.c. has no practical advantage over d.c. in depositing a thicker layer of Li metal (higher capacity) prior to dendrite formation. The main reason for this is that the higher current density applied during p.c. has a lower plating efficiency, and thus faster SEI growth. This faster growth accelerates the depletion of Li^{+} at the Li-SEI interface, thereby bringing about the conditions critical for dendrite initiation (C_{e}^{*} approaching 0) sooner than during d.c.

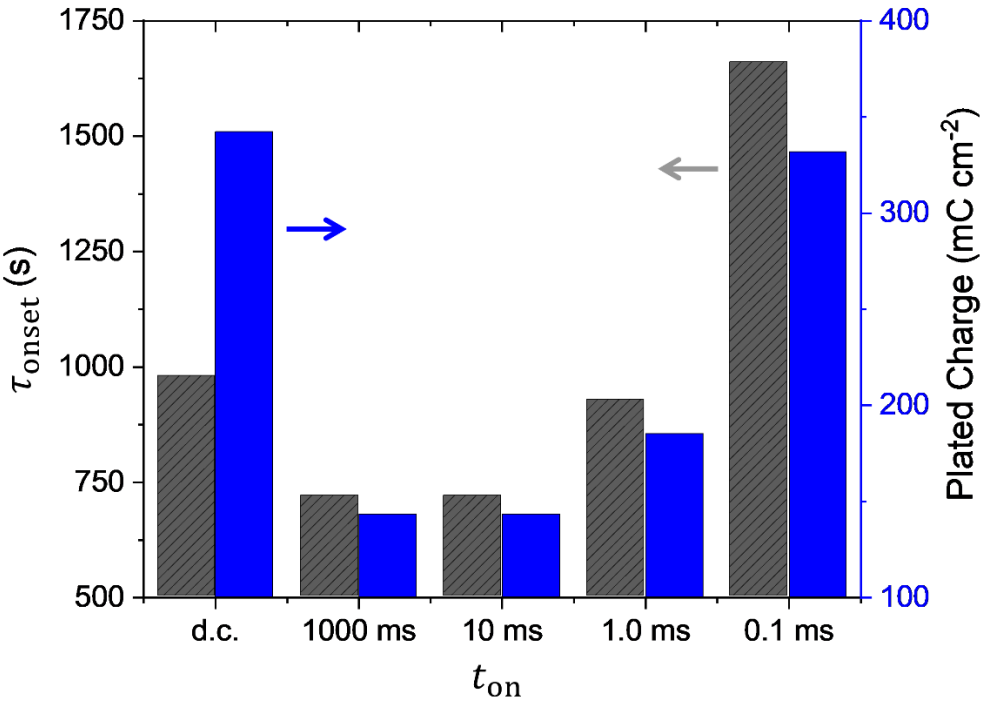

Figure 4.7 - Dendrite onset times (τ_{onset}, *grey*) determined from numerical simulations and their corresponding plated charge densities (Q, *blue*) estimated from Eq. 4.3 for the plating conditions shown in Table 4.1.

4.3 Conclusions

The evolution of the Li^+ concentration profile within the SEI during direct current and pulsed current Li plating were compared using numerical simulations. The following main conclusions are drawn from this chapter:

(i) The numerical results match with the analytical model results for the Li dendrite onset time for d.c. plating.

(ii) The time constant for the development of a linear concentration gradient within the SEI is much less than the time-scale over which SEI growth occurs. This implies that the steady state assumption used in the analytical model (developed in Chapter 2) is valid.

(iii) Pulsed current Li plating at a rate equivalent to d.c. plating can delay dendrite onset time if the length of the pulse is less than the time constant for pseudo-steady state to be established. However, p.c. plating is not able to mitigate the concentration depletion experienced at the Li electrode surface in a way that would benefit the charging of Li-metal batteries. At an equivalent-plating rate relative to d.c. plating, p.c. does not allow more charge to be passed before dendrites initiate. This is because of the increased SEI growth rate during p.c., which accelerates the onset of mass transport limitations on the Li^+ within the SEI.

CHAPTER 5. Conclusions and Future Work

5.1 Summary and Conclusions

The mechanism responsible for Li dendrite initiation was studied using chronopotentiometry, optical imaging, and modeling. It was shown that concentration depletion in the solid electrolyte interphase (SEI) is responsible for the onset of dendritic Li electrodeposition. SEI growth occurred during and prior to Li plating as measured by an increase in the surface overpotential (measured by chronopotentiometry), and surface resistance (measured by EIS). This SEI growth was shown to be responsible for the eventual concentration depletion of Li^+ at the Li metal-SEI interface. The characteristic time τ_{onset} when dendrites first appeared during galvanostatic Li plating was shown to occur at a local maximum in the surface overpotential. The onset time was explained using an analytical transport model. The model allowed qualitative predictions of how τ_{onset} depends on parameters such as initial SEI thickness and current density.

The model for Li dendrite growth was extended to explain the effect of temperature on Li electrodeposition. Temperature-controlled chronopotentiometry and EIS were used to study Li plating over a range of temperatures. It was shown that the onset of dendrites is delayed by an increase in temperature. This effect is due to an increase in the bulk concentration of Li^+ defects within the SEI and/or an increase in Li^+ diffusivity in the SEI. At low temperatures, sluggish Li^+ transport accelerates the depletion of Li^+ at the Li-SEI interface, and this effect causes earlier initiation of Li dendrites.

Numerical modeling was used to examine the details of transient effects at work in Li plating. A diffusion-reaction model was implemented in COMSOL® to study the concentration depletion of Li^+ in the SEI layer. The numerical results for d.c. Li plating were shown to agree closely with the pseudo-steady state analytical model. A comparison of the total charge passed at τ_{onset} was made between pulsed and direct current Li plating to examine if p.c. provides an advantage. Although p.c. plating delays the onset of Li^+ concentration depletion when the pulse is very short (*i.e.*, $<$ 1 ms), this delay does not provide a greater charge before dendrites emerge, when plating Li at an equivalent rate.

In summary, this work emphasizes and begins to unravel the crucial role of Li^+ diffusion through the solid electrolyte interphase (SEI) during the process of Li dendrite initiation. Whereas it was suggested elsewhere that Li dendrites grow due to non-uniformities in the SEI, this work helps to clarify more quantitatively how and at what time Li—even with a relatively uniform SEI—forms dendrites. The presence of Li^+ concentration gradients within a growing SEI drives the initiation of dendritic Li electrodeposition. This framework provides a mechanistic explanation for the effects of critical process parameters (*e.g.*, current density, soak time, temperature, and pulsing) on Li dendrite initiation.

5.2 Outlook and Future Work

Li-metal batteries are a promising candidate for applications that require high-specific energy power sources, such as electric vehicles and electric aircraft. The recharge process for these battery chemistries involves Li electrodeposition on the metal anode. The

present work expounds many of the difficulties associated with Li dendrites, which inhibit the commercialization of Li-metal batteries. In light of the conclusions presented herein, future research efforts targeting Li dendrites should be both fundamental and applied in nature. On the fundamental side, the following opportunities exist for advancing the current understanding of Li dendrites:

(i) *In situ* experimental techniques for measuring SEI thickness are needed. These would help to validate assumptions in the transport model, such as the surface resistance values crucial in determining dendrite onset time, as well as provide a better way to estimate other physicochemical parameters in the model.

(ii) Quantitative analysis using the model requires more precise knowledge of the parameters describing Li^+ diffusion through various components of the SEI. In particular, experimental techniques to measure Li^+ diffusion coefficients and defect concentrations for a given SEI would enable not only greater analytical certainty in the model, but also a means to compare relevant transport properties of a variety of SEI materials directly.

(iii) The results given by numerical simulations in Chapter 4 should be tested experimentally to confirm the prediction that pulsed current Li plating offers negligible, if any, practical advantage for battery charging. It is possible that adjusting the duty cycle could provide greater control, enabling longer (*i.e.*, more practical) pulse lengths to mitigate concentration depletion in the SEI, but this remains to be examined.

Applied research efforts should focus on developing SEI materials that have the following properties: (i) Li^+ transference numbers that are close to unity (suppressing or eliminating Li^+ concentration gradients), (ii) mechanical stability during the volume changes associated with the electrodeposition processes, and (iii) chemical stability in order to prevent continuous growth by electrolyte reduction reactions. Stable materials such as those that avoid solid-state transport limitations within the SEI are desperately needed to advance Li-metal batteries to commercial production. Such SEI materials, if they can be made artificially or formed using electrolyte additives, may hold the promise to prevent the formation of Li dendrites altogether. This technological advancement would help to overcome a major barrier to one of the most promising high-specific energy battery technologies.

APPENDIX A. Li Polarization Experiments on a Rotating Disk

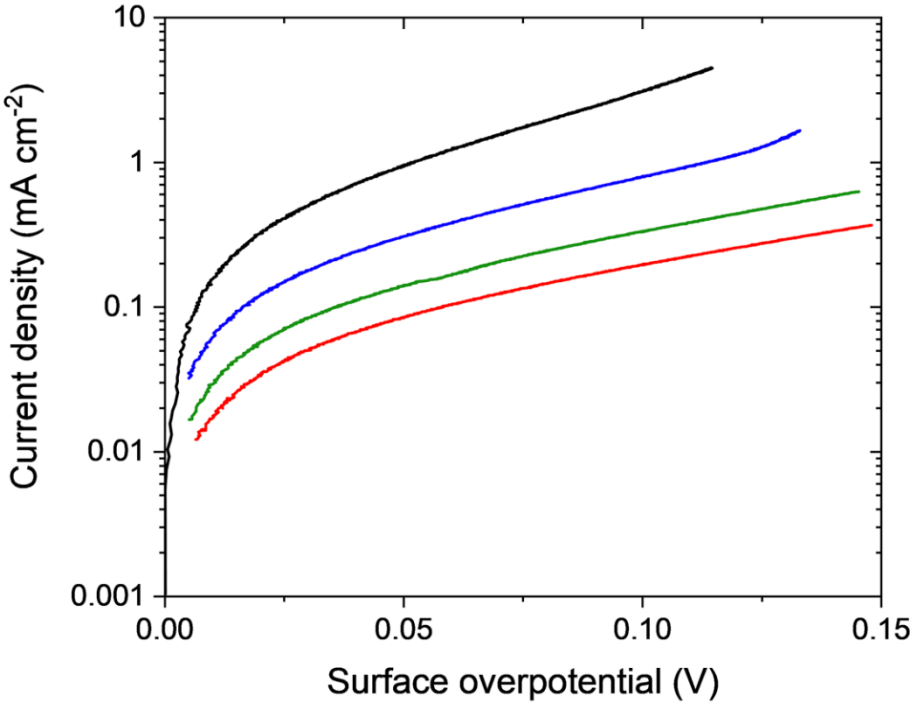

Figure A.1 - Linear sweep voltammetry on Li metal after 6 min (*black*), 30 min (*blue*), 90 min (*green*), and 180 min (*red)* soak times in 1 M $LiPF_6$ 1:1 EC/DMC. The Li surface becomes polarized with increasing soak time due to SEI growth and an increase in R_s. Approximately 1 μm of Li metal was plated onto a 0.5 cm diameter Cu disk prior to polarization measurements. Cu substrates were first polished with 1000 grit sandpaper then 1 μm and 0.3 μm alumina slurries. The WE disk was held in a PTFE shroud (Pine) and rotated at 600 rpm inside an Al beaker filled with 100 mL electrolyte. The Li RE and CE were placed approximately 3.5 cm away from the WE. The potential was scanned from 0 to -0.2 V vs. Li/Li^+ at 2 mV s^{-1}. The surface overpotential η_s was corrected for ohmic loss according to Eq. 2.1.

Bibliography

1. B. Scrosati and J. Garche, *J. Power Sources,* **195,** 2419 (2010).

2. C. Csere, *Car and Driver*, 2013 Tesla Model S Review, www.caranddriver.com/reviews/2013-tesla-model-S-test-review/, accessed Jan. 27, **2017,** (2012).

3. Teslarati Network, *Model S Weight Distribution*, www.teslarati.com/tesla-model-s-weight/, accessed Jan. 27, **2017,** (2013).

4. J. Tarascon and M. Armand, *Nature,* **414,** 359 (2001).

5. D. Linden and T. B. Reddy, *Linden's Handbook of Batteries*, McGraw-Hill, New York (2011).

6. X. Cheng, R. Zhang, C. Zhao and Q. Zhang, *Chem. Rev.,* **117,** 10403 (2017).

7. P. G. Bruce, S. A. Freunberger, L. J. Hardwick and J. Tarascon, *Nat. Mater.,* **11,** 19 (2012).

8. K. J. Harry, D. T. Hallinan, D. Y. Parkinson, A. A. MacDowell and N. P. Balsara, *Nat. Mater.,* **13,** 69 (2014).

9. W. Xu, J. Wang, F. Ding, X. Chen, E. Nasybutin, Y. Zhang and J. Zhang, *Energy Environ. Sci.,* **7,** 513 (2014).

10. M. Wild, L. O'Neill, T. Zhang, R. Purkayastha, G. Minton, M. Marinescu and G. J. Offer, *Energy Environ. Sci.,* **8,** 3477 (2015).

11. J. Yamaki, S. Tobishima, K. Hayashi, K. Saito, Y. Nemoto and M. Arakawa, *J. Power Sources,* **74,** 219 (1998).

12. S. Li, M. Jiang, Y. Xie, H. Xu, J. Jia and J. Li, *Adv. Mater.,* **30,** 1706375 (2018).

13. D. Aurbach, E. Zinigrad, Y. Cohen and H. Teller, *Solid State Ionics,* **148,** 405 (2002).

14. R. Selim and P. Bro, *J. Electrochem. Soc.,* **121,** 1457 (1974).

15. J. B. Goodenough, *Acc. Chem. Res.,* **46,** 1053 (2013).

16. J. Barton and J. Bockris, *Proc. Roy. Soc.,* **268,** 485 (1962).

17. J. Diggle, A. Despic and J. Bockris, *J. Electrochem. Soc.,* **116,** 1503 (1969).

18. C. Monroe and J. Newman, *J. Electrochem. Soc.,* **150,** A1377 (2003).

19. R. Akolkar, *J. Power Sources,* **232,** 23 (2013).

20. X. Cheng, R. Zhang, C. Zhao, F. Wei, J. Zhang and Q. Zhang, *Adv. Sci.,* **3,** 1500213 (2016).

21. R. Cao, W. Xu, D. Lv, J. Xiao and J. Zhang, *Adv. Energy Mater.,* **5,** 1402273 (2015).

22. Z. Liu, Y. Qi, Y. X. Lin, L. Chen, P. Lu and L. Q. Chen, *J. Electrochem. Soc.,* **163,** A592 (2016).

23. J. Jorné and C. Tobias, *J. Electrochem. Soc.,* **121,** 994 (1974).

24. R. Scarr, *J. Electrochem. Soc.,* **117,** 295 (1970).

25. A. N. Dey, *Thin Solid Films,* **43,** 131 (1977).

26. E. Peled, *J. Electrochem. Soc.,* **126,** 2047 (1979).

27. D. Aurbach, Y. Gofer and J. Langzam, *J. Electrochem. Soc.,* **136,** 3198 (1989).

28. K. Kanamura, H. Tomura, S. Shiraishi and Z. Takehara, *J. Electrochem. Soc.,* **142,** 340 (1995).

29. M. Tang and J. Newman, *J. Electrochem. Soc.,* **159,** A281 (2012).

30. G. Bieker, M. Winter and P. Bieker, *Phys. Chem. Chem. Phys.,* **17,** 8670 (2015).

31. C. Wan, S. Xu, M. Y. Hu, R. Cao, J. Qian, Z. Qin, J. Liu, K. T. Mueller, J. Zhang and J. Z. Hu, *ACS Applied Materials & Interfaces,* **9,** 14741 (2017).

32. S. Fouacheayoub, M. Garreau, P. V. S. S. Prabhu and J. Thevenin, *J. Electrochem. Soc.,* **137,** 1659 (1990).

33. Y. Li, K. Leung and Y. Qi, *Acc. Chem. Res.,* **49,** 2363 (2016).

34. N. Kamyab, J. W. Weidner and R. E. White, *J. Electrochem. Soc.,* **166,** A334 (2019).

35. Y. Cohen, Y. Cohen and D. Aurbach, *J. Phys. Chem. B,* **104,** 12282 (2000).

36. D. Aurbach and Y. Cohen, *J. Electrochem. Soc.,* **143,** 3525 (1996).

37. D. Aurbach and Y. Cohen, *Electrochem. Solid State Lett.,* **2,** 16 (1999).

38. J. Steiger, D. Kramer and R. Moenig, *J. Power Sources,* **261,** 112 (2014).

39. G. Liu and W. Lu, *J. Electrochem. Soc.,* **164,** A1826 (2017).

40. C. Monroe and J. Newman, *J. Electrochem. Soc.,* **152,** A396 (2005).

41. C. Monroe and J. Newman, *J. Electrochem. Soc.,* **151,** A880 (2004).

42. P. Barai, K. Higa and V. Srinivasan, *J. Electrochem. Soc.,* **164,** A180 (2017).

43. K. J. Harry, K. Higa, V. Srinivasan and N. P. Balsara, *J. Electrochem. Soc.,* **163,** A2216 (2016).

44. P. P. Natsiavas, K. Weinberg, D. Rosato and M. Ortiz, *J. Mech. Phys. Solids,* **95,** 92 (2016).

45. W. S. LePage, Y. Chen, E. Kazyak, K. Chen, A. J. Sanchez, A. Poli, E. M. Arruda, M. D. Thouless and N. P. Dasgupta, *J. Electrochem. Soc.,* **166,** A89 (2019).

46. C. Brissot, M. Rosso, J. Chazalviel and S. Lascaud, *J. Power Sources,* **81,** 925 (1999).

47. M. Rosso, T. Gobron, C. Brissot, J. Chazalviel and S. Lascaud, *J. Power Sources,* **97-8,** 804 (2001).

48. P. Bai, J. Li, F. R. Brushett and M. Z. Bazant, *Energy Environ. Sci.,* **9,** 3221 (2016).

49. O. Crowther and A. C. West, *J. Electrochem. Soc.,* **155,** A806 (2008).

50. C. Brissot, M. Rosso, J. Chazalviel, P. Baudry and S. Lascaud, *Electrochim. Acta,* **43,** 1569 (1998).

51. A. J. Bard and L. R. Faulkner, *Electrochemical Methods: Fundamentals and Applications*, John Wiley & Sons, New York (2001).

52. K. Nishikawa, T. Mori, T. Nishida, Y. Fukunaka and M. Rosso, *J. Electroanal. Chem.,* **661,** 84 (2011).

53. S. Shi, Y. Qi, H. Li and L. G. Hector Jr., *J. Phys. Chem. C,* **117,** 8579 (2013).

54. J. Christensen and J. Newman, *J. Electrochem. Soc.,* **151,** A1977 (2004).

55. C. T. Love, O. A. Baturina and K. E. Swider-Lyons, *ECS Electrochem. Lett.,* **4,** A24 (2015).

56. M. Ecker, N. Nieto, S. Kaebitz, J. Schmalstieg, H. Blanke, A. Warnecke and D. U. Sauer, *J. Power Sources,* **248,** 839 (2014).

57. D. Lu, Y. Shao, T. Lozano, W. D. Bennett, G. L. Graff, B. Polzin, J. Zhang, M. H. Engelhard, N. T. Saenz, W. A. Henderson, P. Bhattacharya, J. Liu and J. Xiao, *Adv. Energy Mater.,* **5,** (2015).

58. M. Petzl, M. Kasper and M. A. Danzer, *J. Power Sources,* **275,** 799 (2015).

59. E. Peled and S. Menkin, *J. Electrochem. Soc.,* **164,** A1703 (2017).

60. E. Peled, D. Golodnitsky, G. Ardel and V. Eshkenazy, *Electrochim. Acta,* **40,** 2197 (1995).

61. A. Churikov, *Russian J. Electrochem.,* **37,** 176 (2001).

62. A. Churikov, *Electrochim. Acta,* **46,** 2415 (2001).

63. A. Churikov, Y. Kharkats, I. Gamayunova, E. Nimon and A. Shirokov, *Electrochim. Acta,* **46,** 2929 (2001).

64. P. Lu and S. J. Harris, *Electrochem. Commun.,* **13,** 1035 (2011).

65. W. Hagan, N. Hampson and R. Packer, *J. Power Sources,* **24,** 95 (1988).

66. M. Winter, *Z. Phys. Chem.,* **223,** 1395 (2009).

67. M. Hess, *Electrochim. Acta,* **244,** 69 (2017).

68. M. Hess, *J. Electrochem. Soc.,* **165,** A323 (2018).

69. J. Mizusaki, H. Tagawa, K. Saito, K. Uchida and M. Tezuka, *Solid State Ionics,* **53,** 791 (1992).

70. L. Benitez and J. M. Seminario, *J. Electrochem. Soc.,* **164,** E3159 (2017).

71. R. Mogi, M. Inaba, Y. Iriyama, T. Abe and Z. Ogumi, *J. Electrochem. Soc.,* **149,** A385 (2002).

72. H. Ota, X. Wang and E. Yasukawa, *J. Electrochem. Soc.,* **151,** A427 (2004).

73. R. Akolkar, *J. Power Sources,* **246,** 84 (2014).

74. F. Hao, A. Verma and P. P. Mukherjee, *J. Mater. Chem. a,* **6,** 19664 (2018).

75. A. Mistry, C. Fear, R. Carter, C. T. Love and P. P. Mukherjee, *ECS Energy Lett.,* **4,** 156 (2019).

76. H. Sand, *Philos. Mag.,* **1,** 45 (1901).

77. H. Sano, M. Kitta, M. Shikano and H. Matsumoto, *J. Electrochem. Soc.,* **166,** A2973 (2019).

78. Y. Shao, F. Ding, J. Xiao, J. Zhang, W. Xu, S. Park, J. Zhang, Y. Wang and J. Liu, *Adv. Func. Mater.,* **23,** 987 (2013).

79. D. Aurbach, E. Zinigrad, H. Teller, Y. Cohen, G. Salitra, H. Yamin, P. Dan and E. Elster, *J. Electrochem. Soc.,* **149,** A1267 (2002).

80. K. N. Wood, E. Kazyak, A. F. Chadwick, K. Chen, J. Zhang, K. Thornton and N. P. and Dasgupta, *ACS Cent. Sci.,* **2,** 790 (2016).

81. C. Barlow, *Electrochem. Solid State Lett.,* **2,** 362 (1999).

82. J. Thevenin and R. Muller, *J. Electrochem. Soc.,* **134,** 273 (1987).

83. M. E. Orazem and B. Tribollet, *Electrochemical Impedance Spectroscopy*, p. 768, Wiley, New Jersey (2017).

84. A. v. Cresce, S. M. Russell, D. R. Baker, K. J. Gaskell and K. Xu, *Nano Letters,* **14,** 1405 (2014).

85. K. Nishikawa, Y. Fukunaka, T. Sakka, Y. H. Ogata and J. R. Selman, *J. Electrochem. Soc.,* **154,** A943 (2007).

86. D. Aurbach, B. Markovsky, M. Levi, E. Levi, A. Schechter, M. Moshkovich and Y. Cohen, *J. Power Sources,* **81,** 95 (1999).

87. D. Aurbach, Y. Gofer, M. Benzion and P. Aped, *J Electroanal Chem,* **339,** 451 (1992).

88. D. Aurbach and A. Zaban, *J Electroanal Chem,* **348,** 155 (1993).

89. D. Aurbach, M. Moshkovich, Y. Cohen and A. Schechter, *Langmuir,* **15,** 2947 (1999).

90. S. J. Banik. *Suppressing Dendritic Growth During Zinc Electrodeposition Using Polyethylenimine as an Additive for Rechargeable Zinc Batteries*. PhD Thesis, p. 23, Case Western Reserve University, Cleveland, OH (2016).

91. J. Newman and K. E. Thomas-Alyea, *Electrochemical Systems*, Wiley-Interscience, New Jersey (2004).

92. M. Z. Mayers, J. W. Kaminski and T. F. Miller III, *J. Phys. Chem. C,* **116,** 26214 (2012).

93. H. Yang, E. O. Fey, B. D. Trimm, N. Dimitrov and M. S. Whittingham, *J. Power Sources,* **272,** 900 (2014).

94. J. W. Choi and D. Aurbach, *Nat. Rev. Mater.,* **1,** (2016).

95. H. Zhang, G. Gebresilassie Eshetu, X. Judez, C. Li, L. M. Rodriguez-Martinez and M. Armand, *Angew. Chem.,* **57,** 15002 (2018).

96. K. Xu, *Chem. Rev.,* **104,** 4303 (2004).

97. K. Nishikawa, T. Mori, T. Nishida, Y. Fukunaka, M. Rosso and T. Homma, *J. Electrochem. Soc.,* **157,** A1212 (2010).

98. H. Sano, H. Sakaebe and H. Matsumoto, *J. Power Sources,* **196,** 6663 (2011).

99. A. Meitav and E. Peled, *J. Electrochem. Soc.,* **128,** 825 (1981).

100. A. Meitav and E. Peled, *J. Electroanal. Chem.,* **134,** 49 (1982).

101. N. Cabrera and N. Mott, *Rep. Prog. Phys.,* **12,** 163 (1948).

102. E. Markevich, G. Salitra and D. Aurbach, *ACS Energy Lett.,* **2,** 1337 (2017).

103. D. Aurbach, E. Pollak, R. Elazari, G. Salitra, C. S. Kelley and J. Affinito, *J. Electrochem. Soc.,* **156,** A694 (2009).

104. I. A. Shkrob, J. F. Wishart and D. P. Abraham, *J. Phys. Chem.,* **119,** 14954 (2015).

105. R. Bouchet, *Nat. Nanotechnol.,* **9,** 572 (2014).

106. G. Zheng, S. W. Lee, Z. Liang, H. Lee, K. Yan, H. Yao, H. Wang, W. Li, S. Chu and Y. Cui, *Nature Nanotechnology,* **9,** 618 (2014).

107. L. Shi, A. Xu and T. Zhao, *Acs Applied Materials & Interfaces,* **9,** 1987 (2017).

108. A. Basile, A. I. Bhatt and A. P. O'Mullane, *Nat. Commun.,* **7,** (2016).

109. V. Koch, C. Nanjundiah, G. Appetecchi and B. Scrosati, *J. Electrochem. Soc.,* **142,** L116 (1995).

110. D. Aurbach, Y. Talyosef, B. Markovsky, E. Markevich, E. Zinigrad, L. Asraf, J. Gnanaraj and H. Kim, *Electrochim. Acta,* **50,** 247 (2004).

111. B. Purushothaman and U. Landau, *J. Electrochem. Soc.,* **153,** A533 (2006).

112. K. U. Schwenke, S. Solchenbach, J. Demeaux, B. L. Lucht and H. A. Gasteiger, *J. Electrochem. Soc.,* **166,** A2035 (2019).

113. K. N. Wood, M. Noked and N. P. Dasgupta, *ACS Energy Lett.,* **2,** 664 (2017).

114. N. Ibl, *Surf. Tech.,* **10,** 81 (1980).